

Production of Engineered Biochars for Phosphate Removal from Waste Lignocellulosic Materials

First, Second and Third Generation Engineered Products

Michael Ayiania, Sohrab Haghghi Mood, Yaime Jefferson Milan, Manuel Garcia-Perez

Department of Biological Systems Engineering, Washington State University

A report for
The Waste to Fuels Technology Partnership
2017-2019 Biennium: Advancing Organics Management in Washington State



Center for

**Sustaining Agriculture
& Natural Resources**

WASHINGTON STATE UNIVERSITY



DEPARTMENT OF
ECOLOGY
State of Washington

September, 2019

Table of Contents

	<u>Page</u>
List of Figures and Tables.....	ii
Figures.....	ii
Tables.....	iv
List of Abbreviations	vi
Abstract.....	viii
1. First Generation Biochars: Physical Activation with CO ₂	1
1.1 Introduction.....	1
1.2 Materials and Methods.....	2
1.3 Results and Discussion	6
1.4 Conclusions.....	13
2. Second Generation Biochars: Nitrogen Doping	14
2.1 Introduction.....	14
2.2 Methods.....	19
2.3 Results and Discussion	24
2.4 Conclusions.....	35
3. Third Generation Biochars: Nitrogen-Metal Doping.....	36
3.1 Introduction.....	36
3.2 Methods.....	36
3.3 Results and Discussion	38
3.4 Conclusions.....	44
4. References.....	45

List of Figures and Tables

Figures

Figure 1: The Washington State University anaerobic digester biorefinery concept that will make use of the engineered biochar developed in this work (modified from Smith, 2016; Ayiania et al., 2019a)	2
Figure 2: A schematic of the lab-scale pyrolysis and activation reactor used in this study. (Ayiania et al., 2019a).....	3
Figure 3: Installation used for the H ₂ S adsorption test. (Ayiania et al., 2019a)	5
Figure 4: Elemental composition of biochar produced at different temperatures (350°C -800°C). All percentage values are based on bone dry weight.	8
Figure 5: Ash content, volatiles, fixed carbon and moisture content of studied biochar	9
Figure 6: Breakthrough curves of H ₂ S on AD fiber biochar pyrolyzed at different temperatures (500°C to 800°C) (Ayiania et al., 2019a)	10
Figure 7: Adsorption isotherm for phosphate (PO ₄ ³⁻) from (a) 350°C to 600°C, (b) from 650°C, 700°C and Darco activated carbon. Symbols represent experimental data and lines represent the model. Where Q _e is the amount of phosphate adsorbed at equilibrium, C _e is the concentration at equilibrium, and AC350 represent activated carbon produced at 350°C (Ayiania et al., 2019a)..	10
Figure 8: SEM images of biochar before adsorption and after adsorption. (A) is the initial biochar before test, (B) is after H ₂ S adsorption, (C) is after phosphate adsorption. (Ayiania et al., 2019a)	13
Figure 9: Biochar surface functional groups. Where the red and blue balls represent oxygen and nitrogen respectively	18
Figure 10: SEM images of douglas fir wood (a), douglas fir bark (b), and hybrid poplar (c) biochars (magnification 800×, 200× and 300×, respectively) (Suliman et al., 2016).....	19
Figure 11: Summary of CO ₂ activation and nitrogen doping (N-doping) processes used in this report.	20
Figure 12: Experimental set-up used for the production of N-doped char.	21
Figure 13: Mechanism for the formation of N-doped carbons.	21
Figure 14. Top views of the base model surfaces of pristine graphene, graphene nanoribbon terminated with hydrogen, and graphene nanoribbon terminated with hydrogen and oxygen with	

ether functionality. The black and white lines represent carbon and hydrogen, respectively, while the red spheres represent oxygen. The red dashed lines show the supercell boundaries.....23

Figure 15: Experimental set-up for water holding capacity.....24

Figure 16: Surface area of nitrogen-doped chars produced from anaerobically digested fiber treated by CO₂ activation, nitrogen doping (two-step N-doping process: pyrolysis under N₂ gas followed by ammonia activation), or whole process (one-step N-doping process: pyrolysis under ammonia gas).....25

Figure 17: Phosphate adsorption isotherms of chars produced at 750°C from AD fiber. Where CA is biochar activated with CO₂, while ND is nitrogen-doped biochar.26

Figure 18: Top views of nitrogenated defects on the hydrogen-edge graphene model. Top panel shows isolated nitrogen defects (1 nitrogen/20 edge carbon atoms). Species are monomerized pyridinic edge (P₆N-Edge), graphitic nitrogen at the edge (GN-Edge), monomerized pyrrolic without H (P₅N-Edge), monomerized pyrrolic with H (P₅NH-Edge), and graphitic nitrogen at the center (GN-Center).28

Figure 19: Phase diagram of isolated nitrogen functional groups on the hydrogen-edge graphene model with respect to (A) temperature at 1 bar and (B) pressure at 800 K. The perfect hydrogen-edge graphene sheet is the reference structure at $\Delta G = 0$ eV in both graphs.....29

Figure 20: Adsorption isotherms of nitrogen-doped chars produced from cellulose. (A) is N₂ adsorption isotherm and (B) is CO₂ adsorption isotherm31

Figure 21: Effect of addition of raw and N-doped biochar at 2, 5, and 10 wt. % on water holding capacity (WHC) of Quincy sand. PB = particle board feedstock, CO = compost overs feedstock.34

Figure 22: Method used for the production of metal-N-doped chars.37

Figure 23: Surface elemental composition on N-doped char (char doped with only nitrogen), Mg-doped char (char impregnated with magnesium), and Mg-N-doped char (char with both magnesium and nitrogen).....39

Figure 24: XPS spectra of N-doped char and Mg-N-doped char. Figure A is the N 1s spectra where each peak is a different configuration of nitrogen. Figure B is the O 1S where each peak is a different type of oxygen bonding. Figure C is different types of Mg bonding with oxygen, nitrogen and carbon.....39

Figure 25: Structural configurations of individually different types of nitrogen within a coronene model structure. where pyrrolic (edge nitrogen within a five-member ring), pyridinic (edge nitrogen within a six-member ring), graphitic (direct substitution of a carbon atom within a graphite plane), pyridone (edge nitrogen within a six-member ring with one carbon double bonded to oxygen) and N-oxides(edge oxygen double bonded to nitrogen within a six-member ring).....40

Figure 26: Molecular scheme of Mg-N-doped chars within a graphene model structure. Where the first structure is Mg bonded to 4-N within a pyrrolic group. Middle structure is Mg bonded to 3-N within a pyrrolic group and the last structure is Mg bonded to 4-N within a pyridine group.40

Figure 27: Phosphorus Adsorption Isotherm of metal-N-doped chars derived from cellulose.41

Figure 28: Phosphate adsorption by metal and N-doped biochar derived from cellulose (pyrolyzed at 800°C) from solutions of varying initial concentrations. The color intensity is directly proportional to the remaining concentration of phosphate after treatment with biochar for 24 hours, with more intense yellow indicating higher concentrations of phosphate. The photo on the left shows phosphate concentration after being in contact with N-doped biochar (Char_N). The photo in the middle shows solutions that have been in contact with Mg-doped biochar (Char_Mg). The photo on the right shows solutions after contact with Mg-N-doped biochar (Char_Mg_N). The fact that all test tubes are colorless on the right indicates that this biochar has been very effective at removing phosphate ions.....42

Figure 29: Phosphorus adsorption isotherms of Mg-N-doped chars derived from wheat straw ...43

Tables

Table 1: Characterization of Darco activated carbon, raw feedstock (anaerobically digested fiber) and the yield and pH of biochar.7

Table 2: Elemental composition, ash content, yield and phosphate adsorption capacity of biochar derived anaerobically digested fiber.11

Table 3: Composition of metal content and phosphate adsorption capacity of biochar from anaerobic digestion fiber produced at different temperatures.....12

Table 4: N-doped chars from AD fiber that has undergone CO₂-activation (CA), two-step N-doping (ND) under a range of temperatures, and one-step N-doping (pyrolysis under ammonia at 750°C).27

Table 5: Elemental content of N-doped chars from cellulose.....31

Table 6: Surface area (Sa) and pore volume (PV) of N-doped chars from cellulose.32

Table 7: Elemental analysis of municipal solid waste fractions33

Table 8: Proximate analysis of municipal solid waste fractions including moisture content (M wt. %), volatile carbon (VC), fixed carbon (FC), and ash.34

Table 9: Effect of biochar from particle board (PB) and compost overs (CO) on water holding capacity (WHC) of sandy soil.....35

Table 10: Elemental composition of metal-N-doped char derived from cellulose.....	38
Table 11: Result of phosphate adsorption capacity of wheat straw biochar.....	44

List of Abbreviations

AD	Anaerobically digested
Ca	Calcium
CA	Carbon dioxide activation
CEC	Cation Exchange Capacity
CH ₄	Methane
CO	Compost overs feedstock
CO ₂	Carbon dioxide
DFT	Density functional theory
Fe	Iron
FID	flame ionization detector
FWHM	Minimum full width at half maximum
GC	Gas Chromatography Analyzer
GC-MS	Gas chromatography mass spectrometry
HRTEM	High Resolution Transmission Microcopy
H ₂ S	Hydrogen Sulfide
ICP-MS	Inductively coupled plasms mass spectroscopy
Mg	Magnesium
ND	Nitrogen doped
NH ₃	Ammonia
ORR	Oxygen Reduction Reaction
PB	Particle Board
PO ₄ ³⁻	Phosphate ions
SEM	Scanning electron microscopy

TEM	Transmission Electron Microscopy
TGA	thermogravimetric analyzer
VASP	Vienna Ab Initio Simulation
WHC	Water holding capacity
XPS	X-ray photoelectron spectroscopy

Abstract

This report examines several different strategies for creating engineered biochars from waste lignocellulosic materials with enhanced properties chosen specifically for their potential to integrate into urban waste processing biorefineries. Specifically, the goal was to improve capacity for adsorption of phosphates and hydrogen sulfide by chars derived from several lignocellulosic materials including fiber from anaerobically digested dairy manure (AD fiber), urban wood residuals, and wheat straw. The impacts on water holding capacity was also examined as this is an important function for biochar incorporated into soils. In the first generation (CO₂-activated) biochar, a pyrolysis step is followed by an activation step with CO₂. CO₂-activated char from anaerobically digested (AD) fiber had phosphate adsorption capacity of 32.4 mg g⁻¹ biochar. The hydrogen sulfide (H₂S) adsorption capacity of AD fiber-derived chars was 51.2 mg g⁻¹. The breakthrough time for adsorption of hydrogen sulfide for AD fiber-derived char produced at 750°C compared favorably to commercial activated carbon. Second generation biochar was produced using “nitrogen doping” (the process of introducing nitrogen functional groups into a carbonaceous material). When nitrogen-doped char, produced using a single step process had a phosphate adsorption capacity nearly double that of char produced using a two-step process (110.3 mg g⁻¹ vs. 63.1 mg g⁻¹). Our team also conducted analysis of water holding capacity with N-doped biochars produced from urban wood residuals (particle board and compost overs). When raw (non N-doped) char from particle board was blended with Quincy sand soil at a rate of 10% by weight, water holding capacity more than doubled compared to no biochar, from 29.9 to 69.6 % by weight. However, N-doping provided little benefit compared to untreated (raw) biochar, and actually *reduced* the water holding capacity compared to raw biochar at higher application rates. Third generation biochars were produced by impregnating feedstock with metals (Mg, Ca, or Fe) and then using N-doping process to create a metal-N-doped biochar from both pure cellulose and wheat straw feedstocks. Metal-N doping using Mg and N together were effective at improving phosphate adsorption capacity for cellulose char to 335 mg g⁻¹, and from wheat straw to 288 mg g⁻¹. With further development, these processes hold great promise for integration into a municipal biorefinery. For example, activated biochar derived from AD fiber could be used for H₂S removal from AD biogas and phosphate removal from AD effluent. Chars from could be sold and used to adsorb phosphate from a variety of other wastewaters or to reduce H₂S emissions from compost. Within either of these scenarios, the resulting phosphate-charged biochar could perhaps be sold as a nutrient-rich soil amendment, though more information is needed to determine nutrient availability to plants following soil amendment with these materials.

1. First Generation Biochars: Physical Activation with CO₂

Authors' note: This study's results have been published as

Ayiania M, Carbajal-Gamarra FM, Garcia-Perez T, Frear C, Suliman W, Garcia-Perez M: Production and characterization of H₂S and PO₄³⁻ carbonaceous adsorbents from anaerobic digested fibers. *Biomass and Bioenergy*, January 2019, 339-349.

Haghighi-Mood S, Ayiania M, Jefferson-Milan Y, Garcia-Perez M: Nitrogen Doped Char from Anaerobically Digested Fiber for Phosphate Removal in Aqueous Solutions, Paper submitted to *Chemosphere*, 2019

Portions of this chapter, including figures, were taken directly from these publications.

1.1 Introduction

Anaerobic digestion (AD) is a technology that converts organic wastes (e.g., dairy farm manure) into methane (Uludag-Demirer et al., 2008). The process relies on a complex mixture of symbiotic microorganisms (Speece, 1996; Wilkie, 2005). Odor reduction and pathogen control are other benefits of AD (Holm-Nielsen et al., 2009); however, this process also has its drawbacks associated with high concentrations of hydrogen sulfide (H₂S) in the resulting biogas and significant amounts of nutrients (phosphorus [P] and nitrogen [N]) in the resulting liquid effluent (Güngör & Karthikeyan, 2008; Guo et al., 2007; Hobson & Feilden, 1982; Kaparaju & Rintala, 2011; MacConnell & Collins, 2007; Rico et al., 2007). High H₂S concentrations limit biogas use for internal combustion engines (Pelaez-Samaniego et al., 2017) and the presence of P and N in the liquid effluent can be an important source of water pollution if not properly managed (Streubel et al., 2012b; Yao et al., 2011a).

While numerous chemical, physical and biological methods exist for the separation and removal of phosphorus from AD effluents and H₂S from biogas (Kleerebezem & Mendezà, 2002; Nishimura & Yoda, 1997; Soreanu et al., 2008), many of these solutions are problematic from a cost perspective, particularly with respect to annual operating and maintenance expenses (Zhao et al., 2010). Correspondingly, academic research continues with respect to treatment approaches that can minimize cost concerns, preferably through integrated solutions utilizing internal co-products from the AD process. Because the problems of H₂S removal from biogas and phosphate (PO₄³⁻) removal from aqueous effluents are relevant to addressing issues encountered in AD, it is sensible to develop carbonaceous adsorbent materials from the AD fibers generated by these systems. AD fiber can be easily separated and dewatered by screens and screw presses, producing a solid with approximately 30% dry matter, with significant ash content (Teater et al., 2011), and suitable for conversion to char (Yao et al., 2011a). Streubel et al. (Streubel, 2011)

produced a biochar from AD fibers for phosphorus removal from dairy lagoons with an average of 381 mg L⁻¹ P removal. The carbonaceous materials herein developed from AD fibers will be used as part of the bio-refinery concept shown in Figure 1. Because sulfur and phosphorus are plant nutrients, the carbonaceous materials loaded with these compounds have potential to be commercialized as fertilizers (Latos et al., 2011; Lee et al., 2006; Shang et al., 2013; Yao et al., 2011b; Zhang et al., 2016).

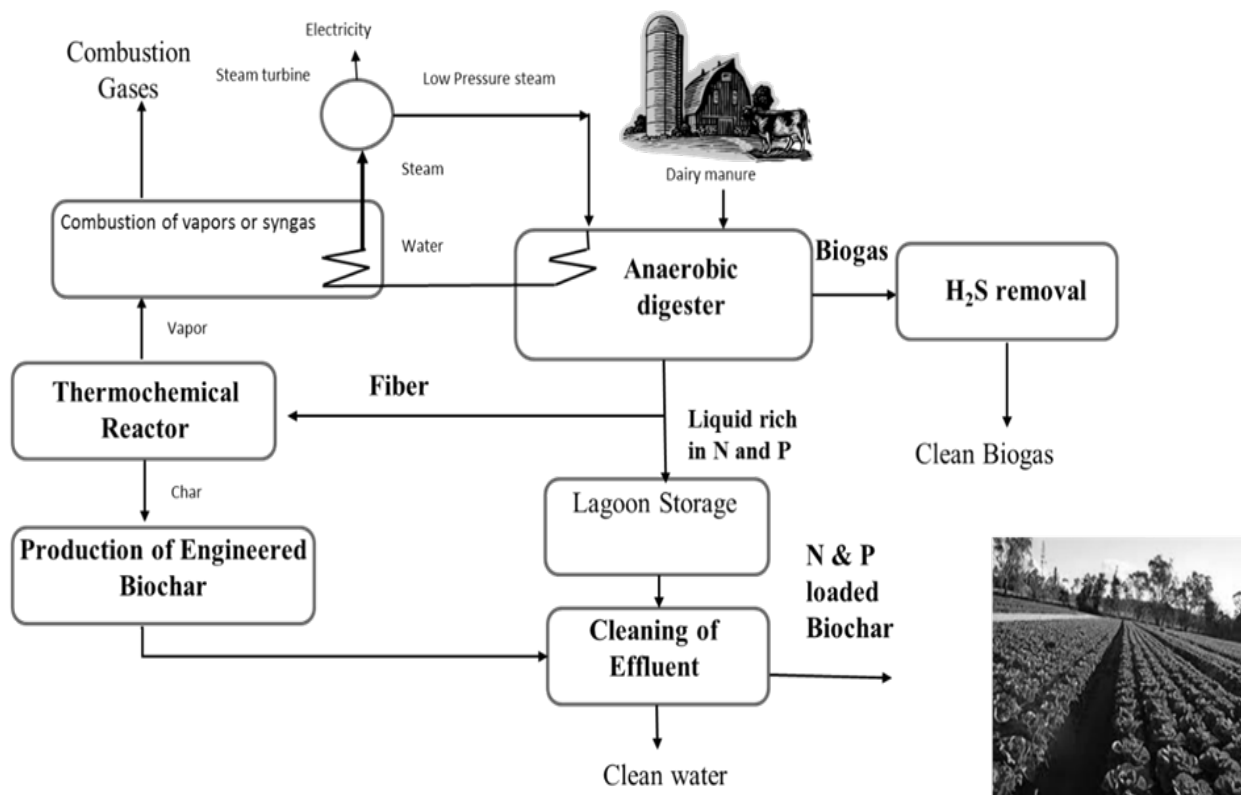


Figure 1: The Washington State University anaerobic digester biorefinery concept that will make use of the engineered biochar developed in this work (modified from Smith, 2016; Ayiania et al., 2019a)

1.2 Materials and Methods

1.2.1 Anaerobically digested fiber collection

Anaerobically digested dairy fiber was collected from George DeRuyter and Sons Dairy Farm in Outlook, Washington. This dairy farm uses a flush handling system, where the dilute manure wastewater is sent to a clarifier before entering a mesophilic, 20-day mixed plug flow anaerobic digester. After digestion, the effluent is sent to a slope screen attached to a dewatering roller, which presses the effluent for mechanical recovery of digested fibrous solids with an approximate moisture content of 72 wt. %. A representative portion of the digested fiber was transferred to Washington State University, where it was partially dried at ambient conditions for

one week. The AD fiber was subsequently dried at 103°C for 24 hours, as described elsewhere (Ferraz et al., 2016). The commercial activated carbon (Darco) used to compare the performance of our biochar was obtained from Cabot Norit Activated Carbon Americas Inc. (Boston, Massachusetts).

1.2.2 Production of biochar and physical activation

A series of biochars were obtained by slow pyrolysis and activation with carbon dioxide (CO₂) at temperatures between 350°C and 800°C from AD fiber in a quartz tube furnace reactor of 50 mm outer diameter (OD) x 44 mm inner diameter (ID) x 1000 mm length (L), (2" D x 40" L) as shown in Figure 2. In this research we used a particle size of approximately 1 mm. Briefly, the about 5 g sample was kept in contact with nitrogen gas (N₂) inside the furnace for 30 minutes at 25°C. After that, the temperature was increased from 25°C to the expected final temperature (350 to 800°C) at a heating rate of 10°C per minute. The sample was kept at the final temperature for two hours. In the first hour the sample was kept under N₂. The sample was then exposed to CO₂ for another hour. Flow rates of 500 mL min⁻¹ and 1000 mL min⁻¹ were employed for N₂ and CO₂, respectively. Samples were then cooled to temperatures below 25°C under nitrogen gas before exposure to air. The activated biochar obtained was characterized and used for the adsorption studies.

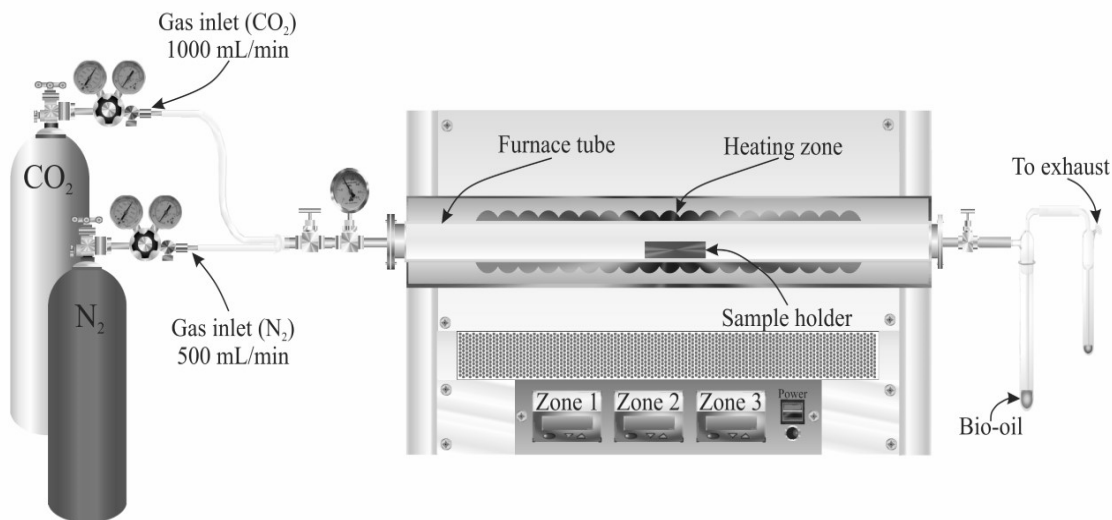


Figure 2: A schematic of the lab-scale pyrolysis and activation reactor used in this study. (Ayiania et al., 2019a)

1.2.3 Anaerobically digested fiber and products characterization

Proximate analysis

Proximate analysis was carried out to determine the moisture content, fixed carbon, volatiles, and ash content of the biochars. This test was done using a thermogravimetric analyzer (TGA) SDTA851e (Mettler Toledo, US). Briefly, moisture content was determined as the weight loss

after the char was heated in a crucible to 120°C and held at this temperature for 3 minutes under nitrogen. Volatile matter was determined as the weight loss after the char was heated to 950°C (under nitrogen) and held for 5 minutes, then cooled down to 450°C. Ash was defined as the remaining mass after the char was subsequently heated to 600°C and held for 8 minutes under oxygen flow.

Elemental analysis

Elemental analysis was performed using a TRUSPEC-CHN® (LECO, US) elemental analyzer (Ferraz et al., 2016). Briefly, 0.15 g samples of biochar were used to determine total carbon (C), nitrogen (N) and hydrogen (H). The oxygen (O) mass fraction was determined by difference (the ash content was taken into account for this calculation).

pH

pH was analyzed following the method described elsewhere (Arenas-Lago et al., 2013). A 0.4 g biochar sample was added to 20 mL deionized water. The suspension was shaken with a mechanical shaker at 40 rpm for 1 hour and equilibrated for 5 minutes before measuring the pH with a pH meter (Fisher Scientific Accumet basic AB15).

Gas physisorption analysis for biochar surface area and porosity

Carbon dioxide (CO₂) adsorption isotherms were measured at 273 K on micromeritics TriStar II PLUS Surface Area and Porosity Analyzer (Norcross, GA, USA). Before each analysis, biochar samples were degassed at 250°C for 18 hours under a vacuum of 0.05—0.1 mbar (the degassing temperature was chosen based on the production temperature of the biochar to avoid sample degradation during preparation). Carbon dioxide (CO₂) adsorption isotherms were measured between the partial pressure range of $p/p^0=10^{-5}$ to $p/p^0=0.03$ using 75 set equilibration points. Surface area and micropore volumes were estimated for CO₂ adsorption using the Dubin-Radushkevich (DR) equation (Dubinin & Radushkevich, 1947; Dubinin et al., 1947).

Morphological analysis

The biochar surface was visualized by scanning electron microscopy (SEM) using a Hitachi S-570 variable pressure instrument. Biochar samples were analyzed before and after adsorption studies using a magnification range of 200x and 2000x. Due to the conductivity of each sample, no preliminary metal coating was required.

ICP-MS

After biochar production, all samples were analyzed for the presence of metals. Metal analysis was conducted based on the method described elsewhere (Pecha et al., 2015), in an inductively coupled plasma mass spectrometry (ICP-MS; Agilent 7500cx) instrument.

1.2.4 Adsorption studies

H₂S Adsorption

A schematic representation of the experimental set up used is provided in Figure 3. The adsorption tests were carried out in vertically-oriented polycarbonate tubes (6.35 mm internal diameter, 250 mm long). In each experiment, 300 mg of activated biochar was packed in the tube. The tests were conducted at atmospheric pressure and room temperature. A simulated biogas containing 2000 ppm of H₂S, 65 vol. % methane (CH₄), and a balance of CO₂ was used for each adsorption trial. H₂S was then passed through the column of adsorbent at a rate of 10 mL min⁻¹ of gas. The flow rate of gas was controlled by a volumetric flow meter. A 0.1 N hydrochloric acid (HCl) solution (500 mL, using domestic water) was employed to humidify the biogas before reaching the column. The concentration of H₂S was monitored using a gas chromatography analyzer (GC; Varian GC3800, equipped with an Agilent CP-SilicaPLOT 50m x 0.53mm x 4μm column) with a computer-automated data acquisition program. The breakthrough concentration was set to be 10% of the initial concentration of H₂S. The simulated biogas used for the analyses contained: 0.1995 vol. % of H₂S, 65.020 vol. % of CH₄, and 34.78 vol. % of CO₂. The activated carbon was allowed to reach saturation before the test was stopped.

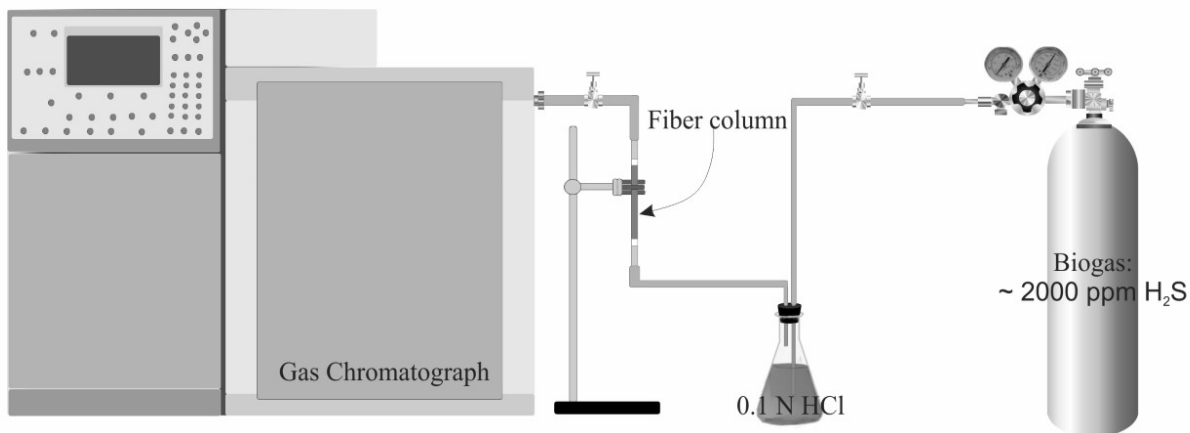


Figure 3: Installation used for the H₂S adsorption test. (Ayiania et al., 2019a)

Batch Equilibrium studies of phosphate adsorption

Biochar samples produced between 350°C to 700°C were tested for capacity to retain phosphate. Sodium phosphate buffer solutions were prepared with nanopure water (> 18 MΩ cm), sodium phosphate monobasic (NaH₂PO₄), and sodium phosphate dibasic (Na₂HPO₄) to guarantee a buffer solution of pH of 7. The concentrations were chosen to represent the range of nutrient concentrations commonly observed in dairy manure effluents (0, 10, 30, 50, 80 and 100 mg L⁻¹). *Adsorption isotherm models:* The experimental results obtained were fitted with the Langmuir isotherm (see Eq. 1.1) and the Freundlich (see Eq. 1.2) models. Isotherm models can give insight into the nature of adsorption and scale up of processes.

The Langmuir model is shown in Eq. 1.1

$$qe = \frac{(Q_{max}K_L C_e)V}{1 + K_L C_e} \quad (\text{Eq. 1.1})$$

Where: Q_{max} ($mg\ g^{-1}$) is the maximum saturated adsorption capacity of activated biochar, C_e (mg/L) is PO_4^{3-} equilibrium concentration, qe ($mg\ g^{-1}$) is the amount of PO_4^{3-} uptake at equilibrium, V (L) is the volume of solution, and K_L is an equilibrium constant related to the affinity between the adsorbent and the adsorbate.

The Freundlich model can be mathematically expressed as shown in Eq. 1.2

$$qe = K_F C_e^{1/n} \quad (\text{Eq. 1.2})$$

Where: K_F is the Freundlich constant ($L\ mg^{-1}$), $1/n$ is a dimensionless Freundlich intensity parameter, and C_e ($mg\ L^{-1}$) is the magnitude of adsorption driving force.

A suspension of 0.2 ± 0.005 g of activated biochar in 25 mL of phosphate buffer solution was formed. The mixture was then placed on a horizontal mechanical shaker and left for 24 hours with duplicates for each concentration. After shaking, the suspension was allowed to stand for at least 2 hours for the particles to settle to the bottom of the tube; the supernatant was later filtered through a $0.45\ \mu m$ filter paper. The equilibrium concentrations of the filtrates from the adsorption studies were measured by a molybdovanadate method using the acid persulfate digestion method (1.0 to $100\ mg\ L^{-1}$) (Hach, 2014a).

1.3 Results and Discussion

1.3.1 Feedstock and Darco activated carbon characterization

Elemental and proximate analyses of the AD fiber used in this study and the commercial activated carbon used for comparison are shown in Table 1. The values obtained for AD fiber are comparable to those found by Sheets et al. (Sheets et al., 2015).

1.3.2 Biochar characterization

The yield of biochar obtained from the AD fiber are shown in Table 1. The biochar yield decreased as the production temperature increased from $350^\circ C$ to $800^\circ C$. This trend is attributed to the removal of volatiles by pyrolysis reactions and by the removal of fixed carbon by oxidation with CO_2 . Pyrolysis is responsible for the weight losses at temperatures below $600^\circ C$, and the reduction in char yield over $600^\circ C$ is mostly due to char oxidation. The high yields of char observed at $600^\circ C$ may be explained by the relatively high content of ash (15.5 wt.%) in the AD fiber. The presence of ash is known to catalyze biochar oxidation (Smith et al., 2017). Biochar pH values varied from 8.0 to 12.0 with pH increasing as a function of production temperature ($350^\circ C$ to $800^\circ C$). This observation is of interest as biochar pH is known to impact

removal of both hydrogen sulfide H₂S and phosphate (Bagreev & Bandosz, 2005; Shang et al., 2016).

Table 1: Characterization of Darco activated carbon, raw feedstock (anaerobically digested fiber) and the yield and pH of biochar.

Analysis of Darco Activated Carbon (dry basis)									
C	H	N	O*	Volatile	Fixed C	Ash	Sa _{N₂}	Sa _{CO₂}	PV _{micro}
(wt. %)	(wt. %)	(wt. %)	(wt. %)	(wt. %)	(wt. %)	(wt. %)	(m ² g ⁻¹)	(m ² g ⁻¹)	(cm ³ g ⁻¹)
54.2	0.7	0.4	1.0	8.9	51.1	40.0	371.8	290.6	0.12

Analysis of raw feedstock (AD fiber) (dry basis)							
C	H	N	O*	Volatile	F.C	Ash	
(wt. %)	(wt. %)	(wt. %)	(wt. %)	(wt. %)	(wt. %)	(wt. %)	
43.1	5.0	2.1	34.3	65.4	19.1	15.5	

Yields and pH of biochar										
T (°C)	350	400	450	500	550	600	650	700	750	800
Yield (wt. %)	72	67	61	54	48	42	35	30	23	17
pH	8	9	9.95	9.85	9.95	10.30	10.50	11.35	12.0	12.0

Sa_{N₂}(m² g⁻¹)- Surface area obtained by using N₂ gas, Sa_{CO₂}(m² g⁻¹)- Surface area obtained by using CO₂ gas

PV_{micro} (cm³ g⁻¹) - Micro pore volume

* Obtained by difference

The elemental analysis of each of the carbonaceous products obtained is shown in Figure 4. The carbon content of the samples remains almost constant for the AD fiber up to approximately 600°C. In lignocellulosic materials with low ash content, carbon content always increases as the pyrolysis temperature increases. The lack of important changes in carbon content in our samples can be explained by its high ash content. The elemental composition of the volatiles seems to be similar to the elemental composition of fixed carbon plus ash fractions. The carbon content decreases too between 600°C and 800°C due to the oxidation of the fixed carbon to produce carbon monoxide (CO) and hydrogen gas (H₂) (Sadhvani et al., 2016). The oxygen content decreases from 19.1 to 5.4 wt. % as production temperature increases. The same effect was not observed for nitrogen content, which remained essentially constant with increase in temperature for all biochar samples. This might be attributed to formation of heterocyclic stable nitrogen

functionalities such as pyridines and pyrroles (Yang et al., 2016). At 800°C, however, we observed an important decrease in nitrogen content.

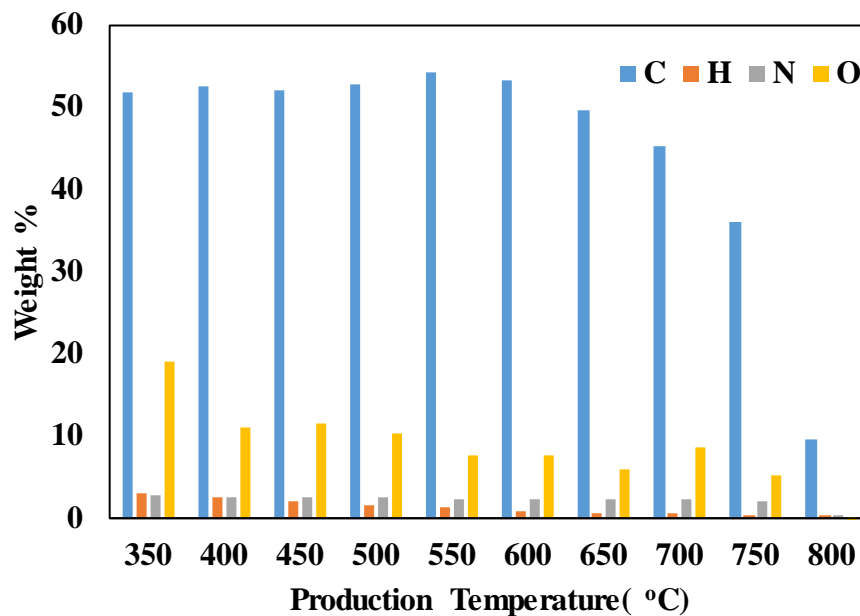


Figure 4: Elemental composition of biochar produced at different temperatures (350°C -800°C). All percentage values are based on bone dry weight.

The proximate analysis of the resulting biochars produced (ash content, volatile matter and fixed carbon) is shown in Figure 5. The ash content in the biochar increases exponentially as production temperature increases. This can be attributed to the accumulation/concentration of the mineral elements during the decomposition of the organic constituents. Meanwhile, the reduction in the fixed carbon at temperatures below 600°C is mostly due to pyrolysis reactions, and at higher temperatures it is attributed to the activation of the biochar with CO₂. The volatile matter decreased with temperature due to volatilization of organic molecules.

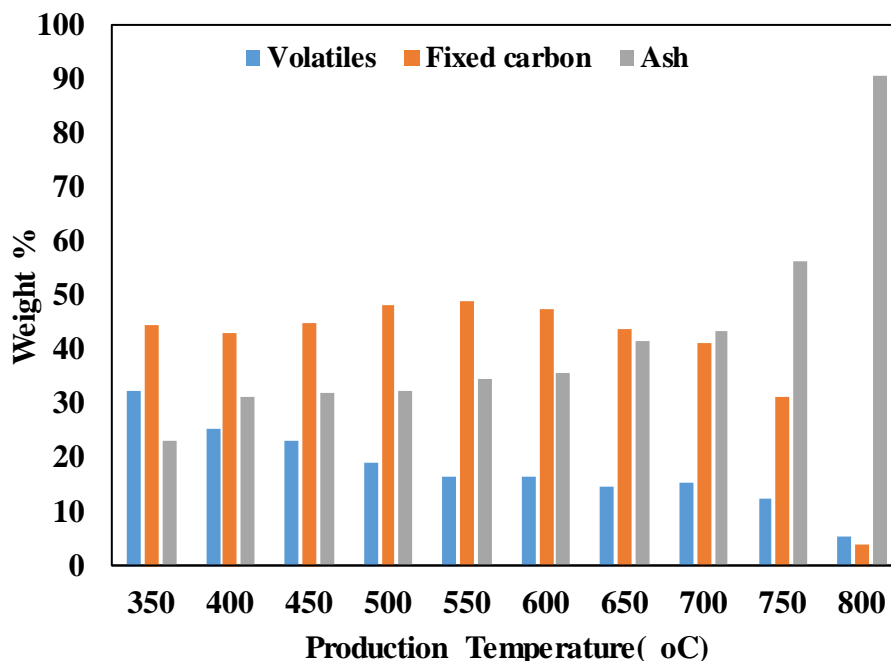


Figure 5: Ash content, volatiles, fixed carbon and moisture content of studied biochar

1.3.3 Adsorption studies

H₂S adsorption studies

The breakthrough results from a thermoseries of activated carbons derived from AD fibers is shown in Figure 6. The breakthrough time is the point on the curve where the effluent of the adsorbate reaches its maximum allowable concentration, which often corresponds to the treatment goal. A longer breakthrough time is preferred. Our results clearly show that the production temperature highly influenced the biochar's capacity for H₂S adsorption. The breakthrough time increased between 500°C and 750°C (surface area: 210 m² g⁻¹ to 305 m² g⁻¹) from 1.0 to 11.0 hours, respectively, while the commercial activated carbon (Darco) took 3.25 hours to breakthrough.

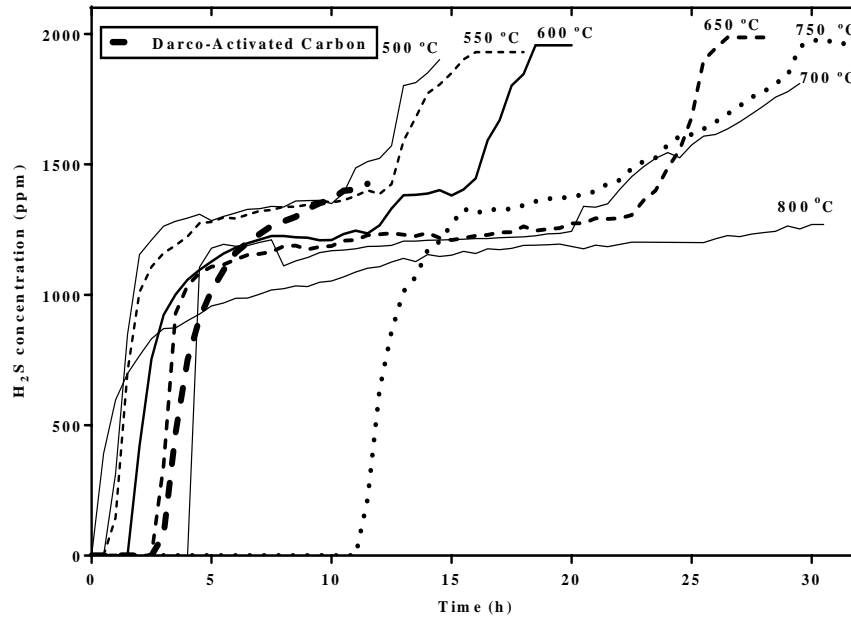


Figure 6: Breakthrough curves of H₂S on AD fiber biochar pyrolyzed at different temperatures (500°C to 800°C) (Ayiania et al., 2019a)

Phosphate adsorption studies

The nonlinear isotherm of the adsorption of phosphate (Figure 7) clearly depicts an increase in the amount of phosphate with respect to temperature from 350°C to 700°C. Adsorption isotherms were used to describe the relationship between phosphate equilibrium concentration and the activated biochar at room temperature. Fitting the Langmuir model to our experimental data enables qualitative assessment the nature of the adsorption process (Foo & Hameed, 2010). The phosphate adsorption capacity of these biochars is shown in Table 2.

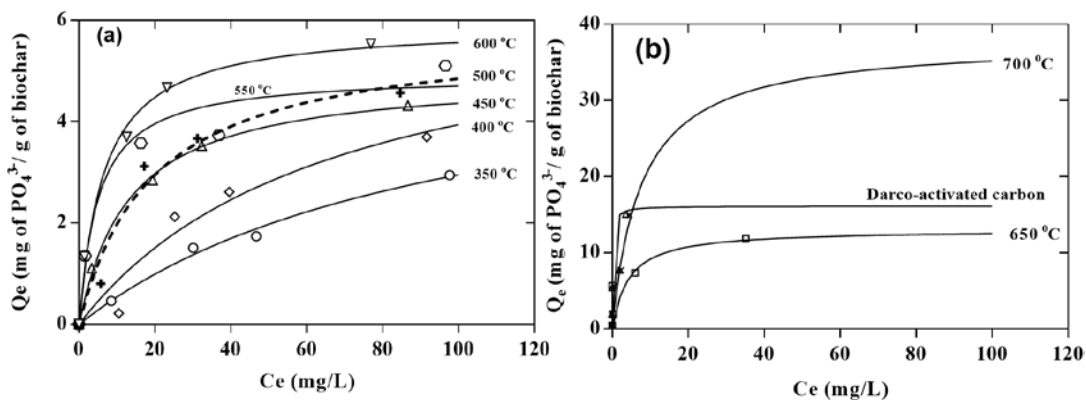


Figure 7: Adsorption isotherm for phosphate (PO_4^{3-}) from (a) 350°C to 600°C, (b) from 650°C, 700°C and Darco activated carbon. Symbols represent experimental data and lines represent the model. Where Q_e is the amount of phosphate adsorbed at equilibrium, C_e is the concentration at equilibrium, and AC350 represent activated carbon produced at 350°C (Ayiania et al., 2019a)

Table 2: Elemental composition, ash content, yield and phosphate adsorption capacity of biochar derived anaerobically digested fiber.

T (°C)	C (%)	H (%)	N (%)	O (%)	Ash (%)	Yield (wt. %)	Langmuir parameters (mg g ⁻¹)
350	51.8	3.1	2.8	19.1	23.1	72	5.8
400	52.5	2.6	2.6	11.0	31.3	67	6.6
450	52.0	2.1	2.5	11.5	31.9	61	4.9
500	52.8	1.7	2.5	10.4	32.6	54	5.8
550	54.2	1.3	2.4	7.6	34.5	48	4.9
600	53.2	0.9	2.4	7.6	35.8	42	5.9
650	49.5	0.6	2.3	6.0	41.6	35	13.1
700	45.2	0.5	2.3	8.6	43.4	30	37.5

The Mg, Ca and Fe content in the biochar and the amount of phosphate adsorbed are shown in Table 3. While the phosphate sorption capacity is similar for lower temperature biochars (350°C to 600°C), the phosphate sorption increases significantly for biochar produced at 650°C and 700°C reaching a maximum adsorption capacity of 37.4 mg PO₄³⁻ g⁻¹ biochar. This behavior is explained by the higher ash content in biochar from AD fiber. When studies were conducted using biochar produced at 750°C, the char completely adsorbed all the phosphate in the aqueous phase (data not presented). This remarkable performance of biochar produced from AD fiber could be due to the presence of mineral content forming a carbon nanoparticle structure which leads to an increase in active sites to retain phosphate. Similar work was done in previous studies, where Mg, Ca, and Fe were doped on the surface of biochar to improve phosphate removal performance (Yao et al., 2013a; Yao et al., 2013b; Zhang & Gao, 2013; Zhang et al., 2012b) and further work on metal N-doped biochar is discussed in chapter 3 of this report. Based on the results with CO₂ activation, 750°C is the best temperature for biochar production for better phosphate retention.

Table 3: Composition of metal content and phosphate adsorption capacity of biochar from anaerobic digestion fiber produced at different temperatures.

T (°C)	mg metal g ⁻¹ biochar			mg PO ₄ ³⁻ g ⁻¹ biochar
	Magnesium (Mg)	Calcium (Ca)	Iron (Fe)	Qe
350	15.9	56.2	1.4	5.8
400	21.5	76.1	1.9	6.6
450	21.9	77.4	1.9	4.9
500	22.3	79.1	2.0	5.8
550	23.6	83.6	2.1	4.9
600	24.6	86.9	2.2	5.9
650	28.5	100.9	2.5	13.0
700	29.8	105.3	2.7	37.4

Scanning electron microscopy (SEM) images providing evidence of structural changes after H₂S and PO₄³⁻ adsorption (Figure 8). Figure 8B (SEM after H₂S adsorption) shows an exfoliated structure due to the formation of sulfuric acid; whereas Figure 8C (SEM after PO₄³⁻ adsorption) shows a structure attributed to possible precipitation of PO₄³⁻ on the surface of the biochar due to the mineral presence.

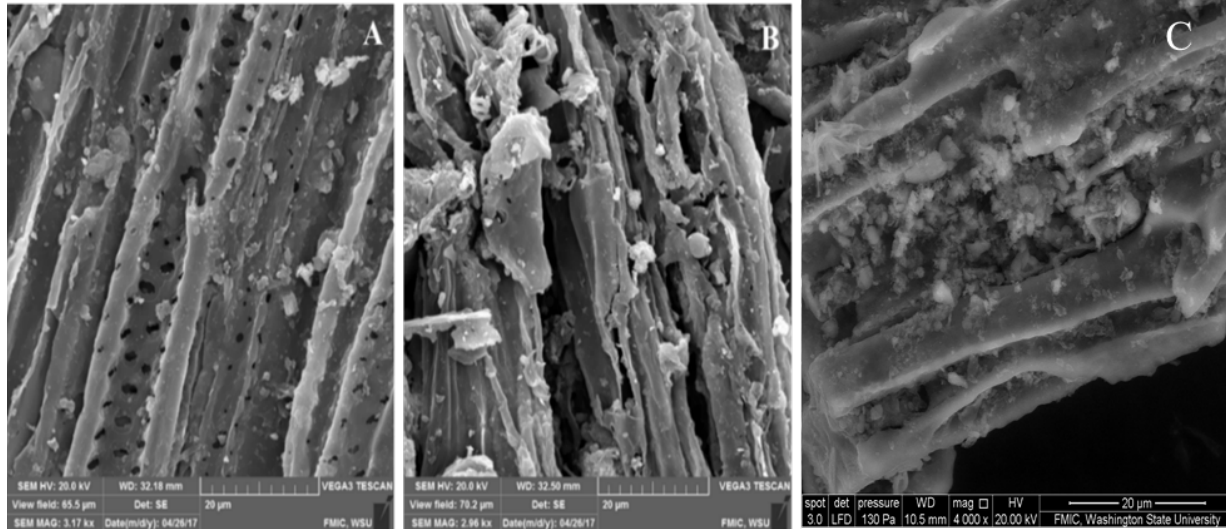


Figure 8: SEM images of biochar before adsorption and after adsorption. (A) is the initial biochar before test, (B) is after H₂S adsorption, (C) is after phosphate adsorption. (Ayiania et al., 2019a)

1.4 Conclusions

The activated biochar produced demonstrated the capacity to adsorb H₂S and phosphate. The production temperature of the biochar had a significant influence on the capacity of the resulting biochar towards H₂S and phosphate adsorption and retention. The adsorption capacity varied between 21.9 and 51.2 mg g⁻¹ for H₂S and between 4.9 mg g⁻¹ and 37.4 mg g⁻¹ for phosphate. Commercially available activated carbon (Darco-Activated Carbon) studied adsorbed 23.1 mg g⁻¹ H₂S and 15.7 mg g⁻¹ PO₄³⁻. The ash content and adsorption in micropores are considered to be the driving forces for these processes. Results of ICP-MS (Inductively coupled plasma mass spectrometry) show high concentration of Mg, Ca, and Fe, which are known to be the main components important for the retention of H₂S and phosphate. This research shows the potential of AD fiber biochar as a remediation material. Therefore, this work shows that the use of activated biochar derived from AD fiber has capacity for H₂S removal from AD biogas and phosphate removal from AD effluent. Also, utilizing the resulting nutrient-rich biochar as fertilizer has the potential to provide social, economic and environmental benefits. Such a holistic approach is needed to unleash the great potentials of thermochemical conversion, anaerobic digestion, and biochar carbon sequestration. Further research is required to standardize the design rules of biochar, which govern feedstock selection and carbonization conditions, leading to desired characteristics for specific pollutant removal capabilities.

2. Second Generation Biochars: Nitrogen Doping

Authors' note: This study's results have been submitted or will be submitted for publication.

Ayiania M, Hensley AJR, Garcia-Perez M, McEwen JS: Thermodynamic Stability of Nitrogen Defects in Carbonaceous Materials from First Principles. Paper Submitted to Carbon, 2019.

Ayiania M, Hensley AJR, Smith M, Scudeiro L, McEwen J-S, Garcia-Perez M: Core Level Binding energy for Nitrogen Doped Char: XPS Deconvolution Analysis through Computational Calculations from first Principles. Paper to be submitted to Carbon, 2019.

Haghighi-Mood S, Ayiania M, Jefferson-Milan Y, Garcia-Perez M: Nitrogen Doped Char from Anaerobically Digested Fiber for Phosphate Removal in Aqueous Solutions, Paper submitted to Chemosphere, 2019.

Portions of this chapter, including figures, were taken directly.

2.1 Introduction

2.1.1 Improving phosphate adsorption capacity of biochar using nitrogen doping

Phosphorus is an essential nutrient for crop growth. However, The release of phosphate from agricultural soils and chemical fertilizers into surface runoff have increased the level of phosphate in water resources (Lalley et al., 2016). Excessive phosphorus in natural waters causes eutrophication and impairs water quality (Boeykens et al., 2017). Moreover, natural reserves of phosphorus are expected to be exhausted within 100 years (Li et al., 2019) . Therefore, it is important to develop technologies to remove and recover phosphate from waste streams. Increasing attention has been paid to develop phosphorus refinery technologies that can recover phosphorus from waste streams, and reuse it (Novais et al., 2018). Dairy manure is a waste streams with high nutrient content. Annually, approximately 350 billion pounds of dairy manure are produced in the US (Cao & Harris, 2010). The economies of scale of dairies offer great opportunities to develop economically viable alternatives for carbon and nutrient management (Jiang et al., 2014). There is general agreement that anaerobic digestion (AD) offers the best opportunities to harness the value of the carbon present in manure through biogas production. Anaerobic digestion reduces odor, solids, and greenhouse gas emissions from raw manure (Zaks et al., 2011). However, AD alone does not offer a solution for nutrient management (Jiang et al., 2014; Streubel et al., 2012a).

Different technologies have been tested for phosphorus removal and recovery such as crystallization, ionic exchange, precipitation, adsorption, and biological phosphorus removal (Antunes et al., 2018; Rittmann et al., 2011; Zhang et al., 2013c). The development of new potential low-cost adsorbents for phosphate recovery has received attention recently (Li et al.,

2016b). Although several studies have reported using montmorillonite, iron oxides, zeolite, pumice, coir pith and red mud as potential adsorbents for phosphate, cheaper more effective adsorbents are required to make phosphate removal economically viable (Chang et al., 2016; Giménez et al., 2007; Jiang et al., 2013; Karimaian et al., 2013; Krishnan & Haridas, 2008; Li et al., 2016b; Ye et al., 2015). Char as a low-cost adsorbent has received increased attention recently. Biomass derived char (biochar) is a carbon-based, porous material produced via pyrolysis in an oxygen-limited environment (Antunes et al., 2018; Suliman et al., 2016; Wang et al., 2015b). Surface functional groups, surface charges and metal content play significant roles in char adsorption properties through physical or chemical interactions between adsorbent and adsorbate (Li et al., 2016a; Vikrant et al., 2018; Yin et al., 2018).

Biochar produced from AD fiber can be a cost-effective approach for phosphate removal (Streubel et al., 2012a). Fiber from AD is not only an inexpensive material, but also it can be recycled and reduce waste in dairies which is consistent with circular economy concept of a circular economy (Pan et al., 2015). The surface of biochar is usually negatively charged and repels negative ions, thus it is difficult to adsorb phosphate (PO_4^{3-} ; (Yin et al., 2018). The functionalization or modification of raw biochar surface is a promising approach to promote affinity towards anionic pollutants (Li et al., 2016a). Acidic functional groups (e.g., hydroxyl, phenol, and carboxyl groups) in char are negatively charged due to the ionization of hydrogen in the solution; therefore, they attract positively charged ions. Positive, basic functional groups (e.g., amides, aromatic amines, and pyridinic groups) are good adsorbents for negatively charged ions (Yin et al., 2017). These basic functional groups can be obtained by “nitrogen doping” (the process of introducing nitrogen functional groups into a carbonaceous material). Nitrogen doping (N-doping) has received much attention recently to improve the performance of carbonaceous materials in different applications such as adsorption, catalysis, and fuel cells (Wang & Chen, 2015; Yang et al., 2015a; Yu et al., 2018).

Ammonia gas (NH_3) could introduce and increase basic nitrogen-containing functional groups on the surface of adsorbent due to reduction of electron-withdrawing acidic group as well as the increase in π electron density and/or oxygen-containing basic groups on the carbon surface (Iida et al., 2013). Yamazaki et al. (2016) treated oxidized polyacrylonitrile fiber with ammonia at 900°C , and ammonization increased the surface area, and adsorption of phosphate significantly. The phosphate adsorption capacity increased from 1.89 to 16.1 mg g^{-1} when ammonia was used. The positive charge of graphitic-N has been found to be effective for adsorption of negative ions such as phosphate and nitrate (Ota et al., 2013). Machida et al. (2016) conducted ammonia treatment to increase positively charged graphitic-N on the activated carbon and achieved a maximum nitrate adsorption capacity of 31 to 37.2 mg g^{-1} .

One of the methods to increase adsorption capacity of char is to generate more pores in the structure of char in order to have more surface area. Physical activation is used most frequently in an oxidizing environment to generate micropores. Commercial choices of activation gas include steam, CO_2 , air, or their mixtures (Zhang et al., 2004). Gasification of the char either with steam or CO_2 or combination of both results in the removal of carbon atoms, in the process simultaneously produce a wide range of pores (predominantly micropores) and generate porous activated carbon (Yang et al., 2010).

The objective of this research was to evaluate and compare the phosphate adsorption capacity resulting from several different strategies for production of CO₂-activated and N-doped chars from AD fiber, cellulose, and municipal solid waste fractions. To achieve this goal, a series of CO₂-activated or N-doped chars were produced. In the case of CO₂-activated char, a pyrolysis step is followed by an activation step with CO₂. Nitrogen doping occurred through either a two-step process – pyrolysis under N₂ gas followed by ammonization (the act of introducing nitrogen groups in a carbonaceous material via reactions with ammonia gas), or through a one-step process involving pyrolysis under ammonia gas.

2.1.2 Stability of structures in N-doped biochar

Carbonaceous materials such as graphene, activated carbon, and amorphous carbons, have garnered great interest in recent years as their physical, chemical, and electronic properties can be finely tuned through functionalization (Dresselhaus & Dresselhaus, 1981; Duesberg et al., 2004; Tsang et al., 2007). Such tuning is accomplished by changing the nature of the organic precursors and the method of activation, which in turn alters the surface chemistry through incorporation of heteroatoms (e.g., oxygen, hydrogen, sulfur, phosphorus, boron and nitrogen) (Bandosz & Ania, 2006; Boehm, 1966; Cruz-Silva et al., 2011; Li et al., 2002; Montes-Morán et al., 2004). Property modification by controlling the surface chemistry of carbon-based materials has been shown to have tremendous technological implications for enhancing the resulting products, including n-type graphene-based field effect transistors (Guo et al., 2010; Lin et al., 2010; Wang et al., 2009; Zhang et al., 2011), electrochemical biosensors (Lv et al., 2012; Lv & Terrones, 2012; Shao et al., 2008; Wang et al., 2010), lithium-ion batteries anodes (Reddy et al., 2010; Wang et al., 2011), heterogeneous catalysts (Deng et al., 2011; Geng et al., 2011; Jafri et al., 2010; Lee et al., 2011; Lefèvre et al., 2009; Lu et al., 2009; Ozaki, 2006; Proietti et al., 2011; Wu et al., 2011; Xu et al., 2018; Yu et al., 2010; Zhang et al., 2006), wastewater treatment (Babel & Kurniawan, 2004; Ban et al., 1998; Hu et al., 1999; Kadirvelu et al., 2003; Liu et al., 2016; Malik, 2004; Wang et al., 2015a; Wang et al., 2008), and trace gas adsorption (Ayiania et al., 2019a; Costa et al., 1981; Reich et al., 1980; Siriwardane et al., 2001; Tamon & Okazaki, 1996).

The value of nitrogen functionalization of graphene has been clearly demonstrated in three areas of application. First, nitrogen functionalized graphene has proven to be a great metal free electrochemical catalyst. It has been extensively used because of its low price, suitable activity for a variety of redox reactions, broad potential window, and relatively inert electrochemistry (Lai et al., 2012; Qu et al., 2010; Tian et al., 2014; Wu et al., 2013; Zheng et al., 2013a; Zhou et al., 2009). Second, in the area of hydrogen storage, graphene is an ideal non-polluting energy carrier with high energy density. The incorporation of nitrogen defects in graphene alone were shown to increase H₂ storage by 66% (Parambath et al., 2012) and H₂ storage was further increased to 124% by combining nitrogen functionalization and palladium (Pd) nanoparticles, where the strong binding of Pd to nitrogen sites maintains the highly dispersed Pd (Giles et al., 2018; Parambath et al., 2012). Finally, the superior performance of nitrogen functionalized graphene at CO₂ storage relative to unmodified graphene was attributed to the strong interaction between nitrogen and CO₂ (Kemp et al., 2013; Saleh et al., 2013) with density functional theory (DFT) revealing strong electrostatic interactions between nitrogen sites and CO₂ due to their strong amphoteric properties (Lee et al., 2015).

There is a wealth of data on the various applications of nitrogen functionalized graphene. However, fundamental knowledge connecting the type of nitrogen structures—i.e. graphitic (direct substitution of a carbon atom within a graphite plane), pyridinic (edge nitrogen within a six-member ring), pyrrolic (edge nitrogen within a five-member ring) — formed during functionalization within a range of temperature and pressure conditions is often limited. Such knowledge gaps at the atomistic level make it difficult to construct experimentally realistic N-doped graphene computational models and molecularly design suitable materials. Some computational studies do not justify their choice of N-doped graphene models (Lambin et al., 2012; Lee et al., 2013; Rad et al., 2015; Zhang et al., 2013a). Other studies, for example, nitrogen active sites in graphene for oxygen reduction reaction (ORR) in fuel cells, base their N-doped model surfaces on the simplest, most common nitrogen structures experimentally observed in an X-ray photoelectron spectroscopy (XPS) analysis of carbonaceous materials (Bhatt et al., 2017; Kim et al., 2011; Li et al., 2014; Liang et al., 2012; Lu et al., 2017; Ma et al., 2012; Yan et al., 2012; Yu et al., 2011; Zhang & Xia, 2011; Zheng et al., 2013b). However, these model choices are complicated by the overlap between the carbon and nitrogen core level binding energies for different nitrogen functionalities, the many possible nitrogen configurations, and the difficulty of controlling the specific nitrogen doping configurations in carbon materials. A number of theoretical studies have explored the stability of different nitrogen configurations in graphene, but such studies do not consistently examine a wide range of nitrogen functionalities over different graphene models and their results are obtained at zero Kelvin and vacuum conditions (Fujimoto & Saito, 2011; Kabir et al., 2016; Yang et al., 2015b; Yin et al., 2016; Zitolo et al., 2015). Experimentally, nitrogen doping is performed under a wide range of temperature and pressure variations, which can significantly affect the types and concentration of nitrogen functionalities incorporated into carbonaceous materials.

In this study, we provide atomistic insight into the most thermodynamically stable nitrogen functionalities in graphene using density functional theory (DFT). We computed Gibbs energies of reaction for the formation of different graphitic, pyridinic, and pyrrolic nitrogen functional groups as a function of temperature and NH_3 pressure on pristine graphene and graphene nanoribbons terminated with either hydrogen or a combination of hydrogen and oxygen. This includes nitrogen incorporation into carbon vacancies and non-hexagonal lattice structures. Activation of carbonaceous materials with ammonia has been described in recent years and was found to act as an activating agent, increasing the porosity of carbonaceous materials with increasing reaction time and temperature (Chen et al., 2005; Mangun et al., 2001). Phase diagrams of nitrogen functionalized graphene showed that nitrogen incorporation was exergonic at graphene edges and that pyridinic functionality was favorable under a wide range of experimental conditions, but thermodynamically competes with graphitic functionality under certain circumstances. Knowledge of the pressure and temperature dependence of nitrogen functionality and concentration in pristine graphene and graphene nanoribbons allows us to effectively tune the graphene electronic properties via treatment conditions. Overall, our work allows for the enhanced design of nitrogenated carbonaceous materials with applications in numerous fields, and the potential to aid in developing process parameters that will add value to biochar by optimizing it for particular purposes.

2.1.3 Improving water holding capacity with N-doped biochar

Biochar has been used as an agent for soil improvement and can influence soil properties and processes. Several studies have shown that the presence of biochar in the soil can increase the availability of nutrients, microbial activity, water retention, and carbon sequestration, while it may reduce fertilizer requirements, greenhouse gas emissions, nutrient leaching, and erosion. The use of biochar in agricultural soils has recently been suggested as an effective tool to reduce the negative impacts of drought, improving soil water holding capacity (Batista et al., 2018).

Use of biochar is a sustainable option to provide long-lasting improvements in soil fertility (Lehmann et al., 2003), especially in sandy soils where agricultural production is constrained due to low water holding capacity and leaching of soil nutrients (Uzoma et al., 2011). Because of its ability to retain nutrients and to improve soil water holding capacity, biochar soil application can be used to overcome some of the limitations faced when land farming sandy soils (i.e., additional requirements for artificial fertilizers and intensive irrigation) providing a promising soil management option for these conditions. Positive effects of biochar on soil properties and plant growth in sandy soil are well documented (Basso et al., 2013; Uzoma et al., 2011). Recent studies have shown that biochar soil additions increase pH of acidic soils, enhance soil cation exchange capacity (CEC), increase soil water-holding capacity (WHC), modify soil bulk density, and increase exchangeable basic cations soils (Basso et al., 2013; Novak et al., 2009; Sika, 2012)

The ability of biochar to improve soil WHC is associated with surface area, surface functional groups, and pore structure of the biochar. The surface area of biochar is generally higher than sand and comparable to clay. Blending biochar with soil raises the total soil surface area, allowing the ability of soils to hold water and retain nutrients (e.g., ammonium, nitrate, P, Mg, and Ca). The presence of polar oxygen-containing surface functional groups raises hydrophilicity of carbon materials aiding the formation of hydrogen bonds, which in turn will impact the ability of water to wet biochar surfaces (see Figure 9). The pore structure of biochar is important for its functionality. The adsorption process occurs mostly in micropores. However, macro and mesopores play important roles in the adsorption process where they act as channel for adsorbate to reach the micropores [Figure 10; (Mohamed et al., 2016)].

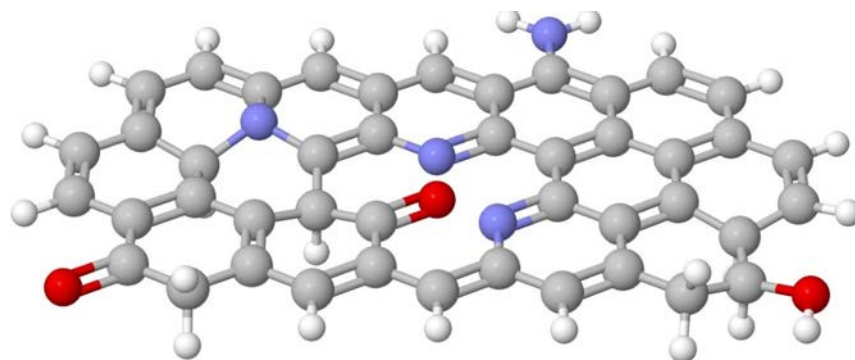


Figure 9: Biochar surface functional groups. Where the red and blue balls represent oxygen and nitrogen respectively

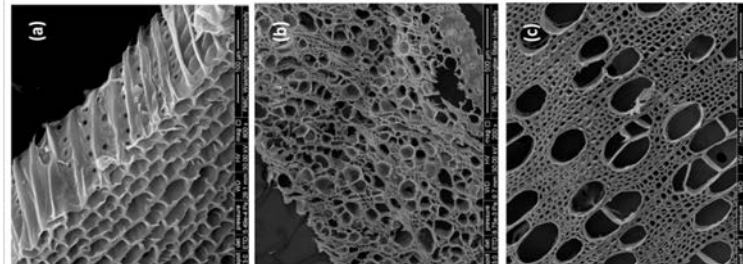


Figure 10: SEM images of douglas fir wood (a), douglas fir bark (b), and hybrid poplar (c) biochars (magnification 800 \times , 200 \times and 300 \times , respectively) (Suliman et al., 2016)

A few studies exist on the effects of biochar porosity and surface functionalities (oxygen functionalities) on the hydro-physical properties of a sandy soil. Oxidized biochar has been demonstrated to increase water retention. The increase in soil water retention when oxidized biochars were added into the soil can be explained by the increase in the oxygen function groups on the surface of these biochars. However, little knowledge exists on the effects of nitrogen functionalities on the WHC of biochar in soil.

In this part of the project, raw biochar and N-doped biochar were produced from two fractions of municipal solid waste - particle board and compost overs (the large woody fraction remaining after composting). These biomass sources were chosen to run the WHC analysis due to their lower concentration in heavy metals compared to other municipal solid waste fractions tested (Ayania et al. 2019b). When using biochar from municipal solid waste fractions as soil amendment, it is very important to consider the heavy metal content to prevent contamination to the soil.

2.2 Methods

2.2.1 N-doped biochar production

Anaerobically digested dairy fiber was separated from a mesophilic mixed plug-flow digester located at Edaleen Dairy in Lynden, Washington. The AD fiber was air dried to a moisture content of 8% by weight, and particle size of 1 mm was used for this study. Three different series of N-doped char were produced from AD fiber, by the use of N₂ or ammonia gas at different stages of the process (Figure 11). 1.) char pyrolyzed under N₂ and activated with CO₂, 2.) char pyrolyzed under N₂ and activated with ammonia after pyrolysis, and 3.) char pyrolyzed with ammonia.

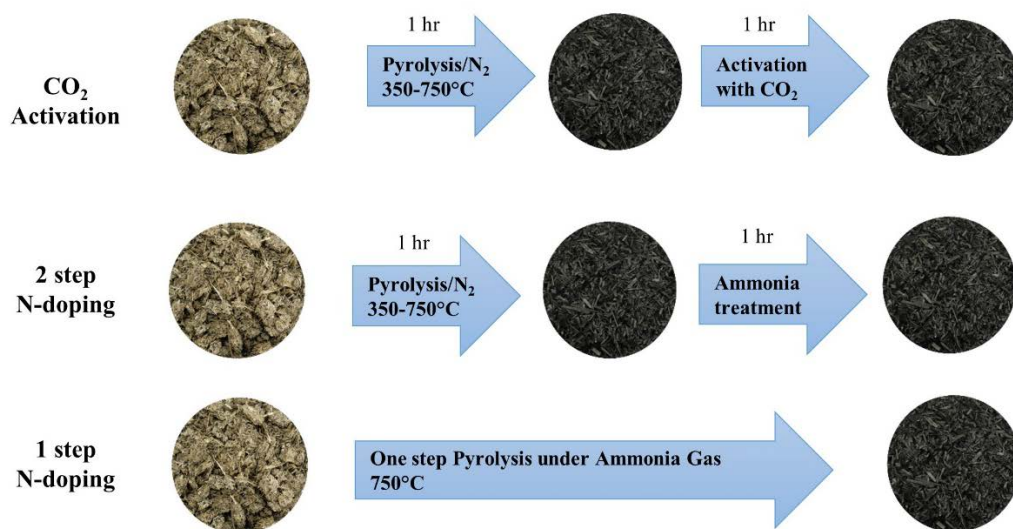


Figure 11: Summary of CO₂ activation and nitrogen doping (N-doping) processes used in this report.

The N-doped char was produced through treating with ammonia at temperatures between 350°C and 750°C in a quartz tube furnace reactor of 50 mm outer diameter (OD) x 44 mm inner diameter (ID) x 1000 mm length (L) (2"Dx40" L; Figure 12). The heating up period was conducted under an oxygen free atmosphere by purging the reactor with N₂. Briefly, AD fiber was kept in tubular furnace in contact with N₂ for 30 minutes at 25°C. Then, the temperature increased from 25°C to desired temperatures (350°C to 750°C) at a heating rate of 10 °C per minute and kept at desired temperatures for two hours. In the first hour, AD fiber was carbonized under the N₂ gas environment. The first series of char (four different chars produced at temperatures from 350°C to 750°C) were exposed to CO₂ to be activated physically for one hour. The second series were treated by ammonia gas also for one hour. The reaction mechanism can be seen in Figure 13. Flow rates of 500 mL min⁻¹ for N₂ and 1000 mL min⁻¹ for CO₂ and ammonia gas were employed, respectively. The char samples were then cooled down to 25°C under N₂. The third type of char (ADF-ND Whole process) was produced under ammonia at 750°C. Briefly, AD fiber was kept in tubular furnace in contact with Ammonia for 30 minutes at 25°C. Then, the temperature increased from 25°C to 750°C at a heating rate of 10°C per minute and kept at desired temperatures for one hour. The same whole process method under ammonia was employed to produced char using cellulose as feedstock.

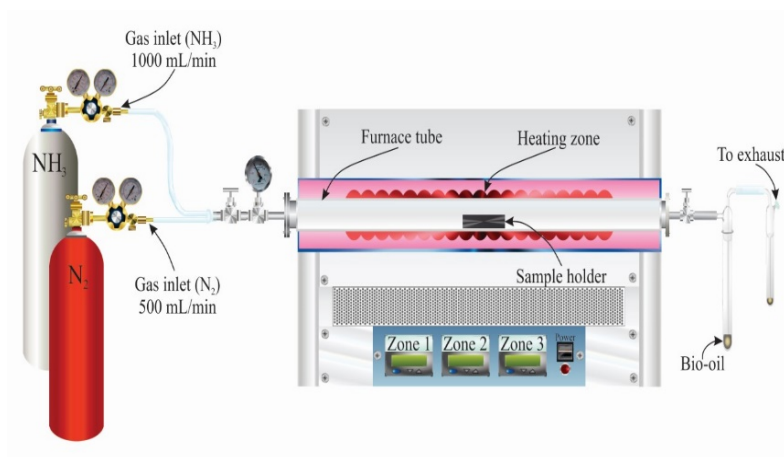


Figure 12: Experimental set-up used for the production of N-doped char.

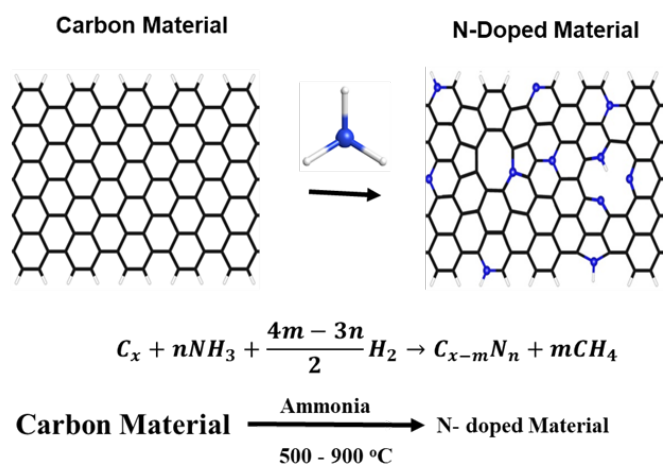


Figure 13: Mechanism for the formation of N-doped carbons.

2.2.2 Phosphate adsorption study

Adsorption isotherm of phosphate on the char was determined by mixing 0.03 g of char with 45 mL of phosphate solutions of different concentrations ranging from 10 to 100 mg·L⁻¹ in the tubes. Phosphate solutions were prepared by dissolving potassium phosphate monobasic (KH₂PO₄, Fisher Scientific) in deionized water. The tubes were shaken in the mechanical shaker for 24 hours at 25°C temperature to reach adsorption equilibrium. The samples were then withdrawn and filtered through a 0.45 μm filter to determine adsorbed phosphate concentrations. pH of solutions was measured with a pH meter (Mettler Toledo, SevenEasy S20) before and after phosphate sorption. Phosphate adsorptions were calculated on the basis of the initial and final aqueous concentrations, which were determined by a molybdovanadate method using the acid persulfate digestion method (1.0 to 100 mgL⁻¹) (Hach, 2014b).

2.2.3 Computational methods for determining stability of nitrogen structures

Density functional theory calculations were carried out using the Vienna *Ab Initio* Simulation Package (VASP) (Kresse & Furthmüller, 1996a; Kresse & Furthmüller, 1996b; Kresse & Hafner, 1993). The projector-augmented wave (PAW) method (Hensley et al., 2018; Kresse & Joubert, 1999) was used to model the core electrons (POTCARs released in 2002 for C, N, and O and 2001 for H) and a plane-wave basis set with an energy cutoff of 450 eV were used to model the valence electrons. To model the electron exchange and correlation, the Perdew-Burke-Ernzerhof (PBE) functional (Perdew et al., 1996) was applied. Spin polarization was included in all calculations. The Gaussian smearing method was used to set partial occupancies of bands with a smearing width of 0.2 eV to facilitate Brillouin zone integration convergence, followed by extrapolation to zero Kelvin for total energy calculation (Gerber et al., 2010; Isvoranu et al., 2009). All ground state optimizations used the conjugate gradient method and were considered converged when relaxed interatomic cartesian forces were smaller than 0.010 and 0.025 eV/Å, respectively. The energy tolerance was set to 10^{-7} eV. Calculations for molecules in the gas phase were performed using an $18 \times 19 \times 20$ Å box using one single **k**-point, the Gamma point, to span the Brillouin zone.

Nitrogen functionalization was studied in three different graphene models (Figure 14): a pristine graphene sheet ($14.8 \times 14.8 \times 20$ Å), a graphene nanoribbon with hydrogen terminated edges ($17 \times 29 \times 21$ Å), and a graphene nanoribbon with a mixture of hydrogen and oxygen terminated edges ($17 \times 29 \times 21$ Å). The graphene lattice constant was 2.467 Å, consistent with previous results (Hou et al., 2012; Mehmood et al., 2013; Pulido et al., 2011). The integration of the Brillouin zone was conducted using a $(3 \times 3 \times 1)$ Monkhorst-Pack grid (Monkhorst & Pack, 1976) for pristine graphene, while a $(1 \times 2 \times 3)$ Monkhorst-Pack grid was used for the graphene nanoribbon models. All structures were visualized using VESTA (Momma & Izumi, 2011).

The choice of defects here was informed by the work of Smith et al. who demonstrated the presence of defects such as vacancies, pentagonal and octagonal structures, and nitrogen defects in amorphous carbons derived from lingo-cellulosic materials (Smith et al., 2016a; Smith et al., 2016b). The carbon defects studied here were the most populous defects and have been imaged with High Resolution Transmission Microcopy (HRTEM), a valuable tool to study and generate defects and monitor structural reconstructions in carbon nanostructures (Rodriguez-Manzo & Banhart, 2009; Terrones et al., 2000; Ugarte, 1992). Banhart and Krasheninnikov have reviewed, theoretically and experimentally, how the electron beam of a transmission electron microscope (TEM) interacts with carbon nanostructures, changing their morphology via the generation, migration, and reconstructions of defects (Krasheninnikov & Banhart, 2007). Types of defects include mono- and di-vacancies and stone-wales defects (Chuvilin et al., 2009; Denis, 2013; Gass et al., 2008; Hashimoto et al., 2004; Lee et al., 2005; Meyer et al., 2008; Warner et al., 2008). Evidence of such carbon defect structures have also been experimentally demonstrated by Iijima and coworkers (Hashimoto et al., 2004). Structures found to be common in the preceding study were examined here.

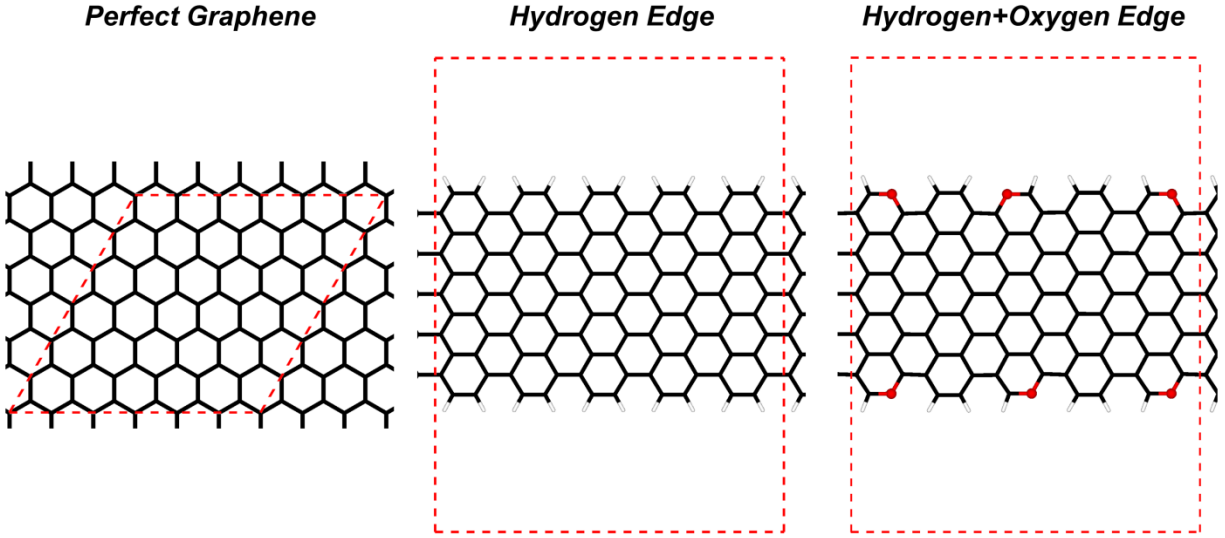


Figure 14. Top views of the base model surfaces of pristine graphene, graphene nanoribbon terminated with hydrogen, and graphene nanoribbon terminated with hydrogen and oxygen with ether functionality. The black and white lines represent carbon and hydrogen, respectively, while the red spheres represent oxygen. The red dashed lines show the supercell boundaries.

The stability of all structures was determined via the calculation of Gibbs reaction energy according to:

$$\Delta G_{\text{rxn}} = E_{\text{rxn}} + \Delta\mu_{\text{CH}_4} - \Delta\mu_{\text{NH}_3} - \Delta\mu_{\text{H}_2} + G_{\text{vib,defect}} - G_{\text{vib,intact}} \quad (\text{Eq. 2.1})$$

In this equation, E_{rxn} is the zero-point corrected DFT reaction energy for the formation of the nitrogen doped structure within the specific graphene sheet model. $\Delta\mu_i$ is the chemical potential of the relevant gas phase species, calculated according to:

$$\Delta\mu_i(T, P) = \Delta\mu_i(T, P_0) - k_B T \ln\left(\frac{P}{P_0}\right) \quad (\text{Eq. 2.2})$$

$$\Delta\mu_i(T, P_0) = [H(T, P_0) - H(0 \text{ K}, P_0)] - T[S(T, P_0) - S(0 \text{ K}, P_0)] \quad (\text{Eq. 2.3})$$

Where T , P , P_0 , k_B , H , and S are the temperature, pressure, reference pressure (1 bar), Boltzmann's constant, and gas phase enthalpies and entropies, respectively. The thermodynamic data required to calculate the chemical potentials as a function of pressure and temperature was taken from the JANAF thermochemical tables (Chase et al., 1974). The gas phase composition was treated as 97 mol% NH_3 , 1 mol% CH_4 , 1 mol% H_2 , and 1 mol% O_2 .

2.2.4 Water holding capacity

The purpose of this experiment was to determine the effect of the biochar produced (both N-doped and undoped) on water-holding capacity of a sandy soil. The undoped biochar was produced under only nitrogen gas whereas the N-doped biochar was obtained by using the two

step method (pyrolysis under nitrogen gas (N₂) and activation under ammonia gas(NH₃). Two feedstocks from municipal solid waste were used (particle board and compost overs (from royal organics) due to their lower content of heavy metals, compared to other woody fractions of municipal solid waste. Sandy soil (Quincy sand) was mixed with N-doped biochar and undoped N-biochar. The experiment set-up is shown in Figure 15. Note that the tests were done in duplicates and the values reported in Table 9 are mean values.

WHC of only biochar WHC of Soil + 2% biochar



Figure 15: Experimental set-up for water holding capacity.

The water holding capacity was conducted using the following procedure described elsewhere (Agvise Laboratories, n.d.). Briefly,

1. Mix 30 g of soil with 2 wt. %, 5 wt. % and 10 wt. % biochar and weigh to the nearest 0.01 g;
2. Add water 50 ml and let drain for 48 hours and later weigh the wet samples;
3. Dry the sample at 105°C for 24 hours and weigh the dry sample; and
4. Calculate the water holding capacity (WHC %) = $((M_{wet}-M_{dry})/M_{wet}) * 100$

2.3 Results and Discussion

2.3.1 Nitrogen-doped char from anaerobically digested fiber

Surface area and pore volume at different temperatures resulting from CO₂ adsorption of CO₂-activated and N-doped chars are shown in Figure 16. The surface area and the micropore volume of the CO₂ activated char increased from 156.5 m² g⁻¹ to 413.1 m² g⁻¹ and from 0.062 cm³ g⁻¹ to 0.165 cm³ g⁻¹, respectively, as pyrolysis temperature increased. Similarly, the surface area and the micropore volume of the N-doped char developed from 166.6 to 463.1 m² g⁻¹ and 0.068 to 0.185 cm³ g⁻¹ as pyrolysis temperature increased. The results indicate that the N-doped chars have slightly more surface area than CO₂-activated chars. Activation of carbonaceous materials with ammonia and its effect on pore structure has been described in recent years. It was found

that ammonia acted as an activating agent and increases the porosity of carbonaceous materials with increasing activation time and temperature (Chen et al., 2005; Mangun et al., 2001). However, the surface area in the the ADF-ND whole process (or one-step) char decreased as compared to the other processes.

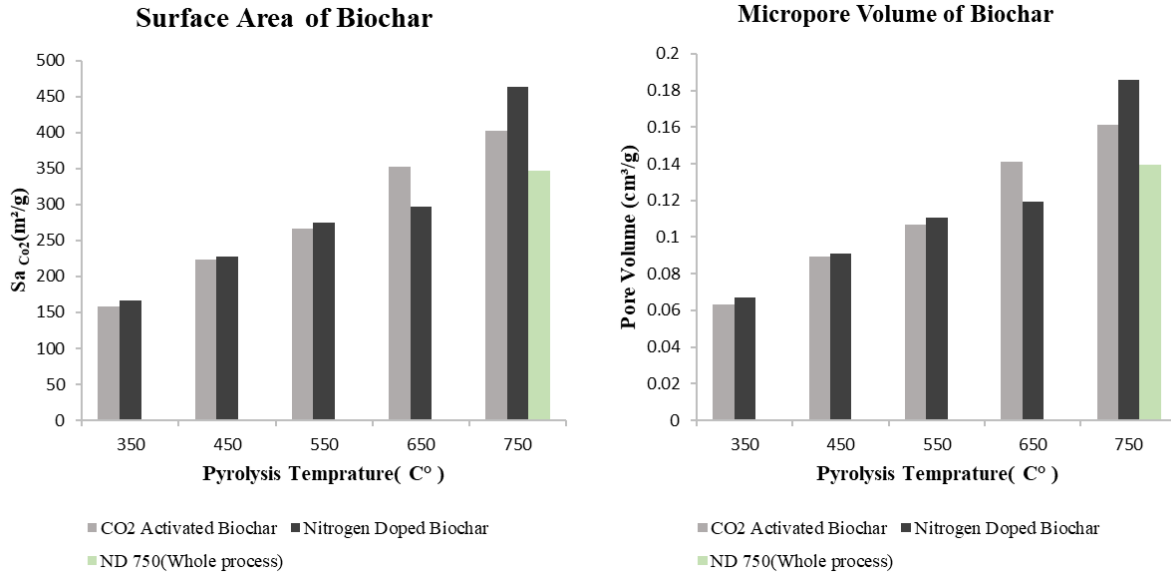


Figure 16: Surface area of nitrogen-doped chars produced from anaerobically digested fiber treated by CO₂ activation, nitrogen doping (two-step N-doping process: pyrolysis under N₂ gas followed by ammonia activation), or whole process (one-step N-doping process: pyrolysis under ammonia gas).

Adsorption isotherms of PO₄³⁻ are shown in Figure 17. In our analysis, we used the four isotherms commonly used to describe char adsorption capacity (Langmuir, Freundlich, Langmuir-Freundlich, and Redlich-Peterson):

$$q = \frac{K Q C_e}{1 + K C_e} \quad \text{Langmuir} \quad (\text{Eq. 2.4})$$

$$q = K C_e^n \quad \text{Freundlich} \quad (\text{Eq. 2.5})$$

$$q = \frac{K Q C_e^n}{1 + K C_e^n} \quad \text{Langmuir-Freundlich} \quad (\text{Eq. 2.6})$$

$$q = \frac{K C_e}{1 + a C_e^n} \quad \text{Redlich-Peterson} \quad (\text{Eq. 2.7})$$

K (L mg⁻¹) and Q (mg g⁻¹) in the Langmuir equation represent the Langmuir bonding term related to interaction energies and Langmuir maximum capacity, respectively, and C_e (mg·L⁻¹) in all isotherms is equilibrium solution concentration of the sorbate. K (mg⁽¹⁻ⁿ⁾ Lⁿ·g⁻¹), and n (dimensionless) in Freundlich denote Freundlich affinity coefficient and the Freundlich linearity

constant respectively. K ($L^n \text{ mg}^{-n}$) and n represent the Langmuir–Freundlich affinity parameter and the index of heterogeneity, respectively. K ($L \text{ g}^{-1}$), a ($L^n \text{ mg}^{-n}$) and n in Redlich–Peterson equation are Redlich–Peterson isotherm constants. The adsorption capacities measured are shown in Table 4. The adsorption capacity of the CO_2 activated and N-doped materials increased in both cases with activation temperatures. The phosphate adsorption capacity increased close to 1.9 times with N-doping.

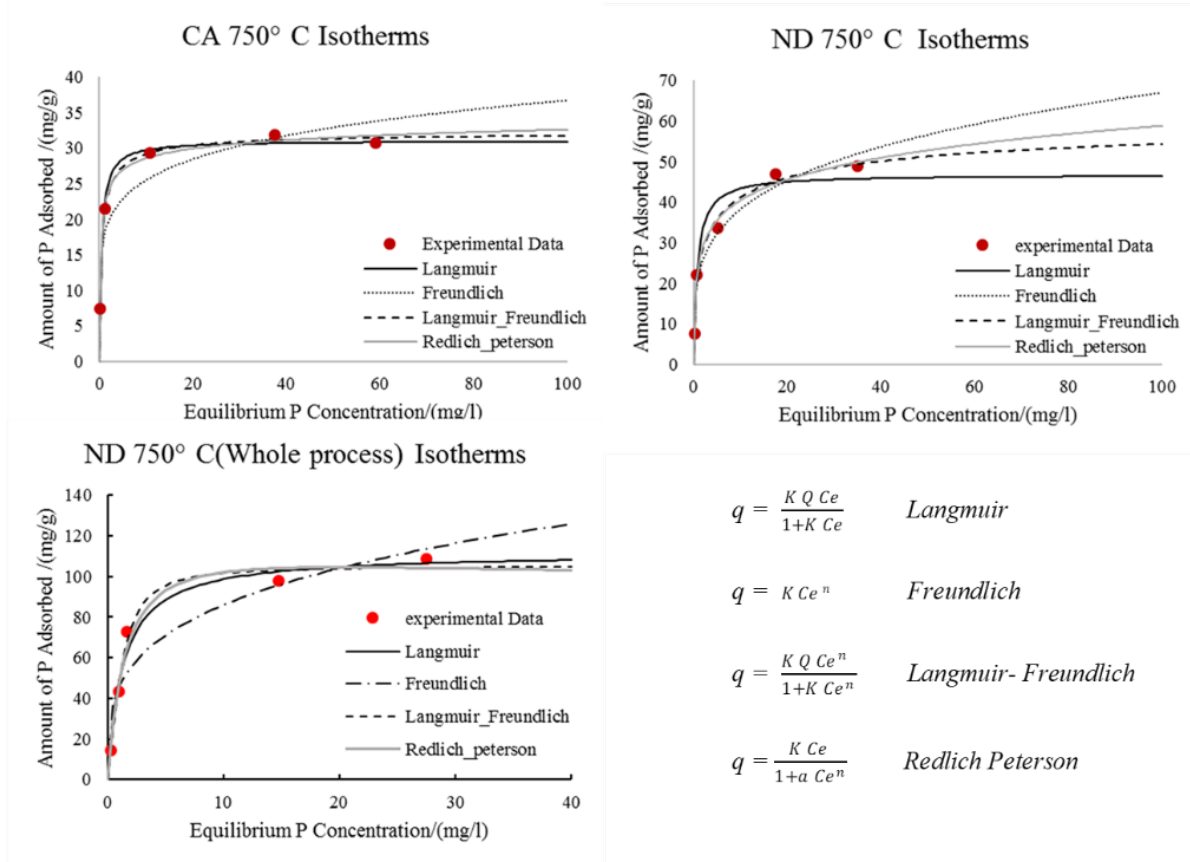


Figure 17: Phosphate adsorption isotherms of chars produced at 750°C from AD fiber. Where CA is biochar activated with CO_2 , while ND is nitrogen-doped biochar.

Table 4: N-doped chars from AD fiber that has undergone CO₂-activation (CA), two-step N-doping (ND) under a range of temperatures, and one-step N-doping (pyrolysis under ammonia at 750°C).

Process	T(°C)	C(%)	H(%)	N(%)	O(%)	Ash(%)	Yield(wt.%)	Langmuir-Freundlich phosphate adsorption capacity (mg g ⁻¹)
CA	350	60.2	3.1	2.5	18.9	15.3	41.4	3.4
CA	450	62.7	2	2.5	14	18.8	35.4	4.9
CA	550	64	1.3	2.3	10.8	21.7	32.7	7.2
CA	650	63.3	0.4	2.4	11.1	22.7	30.6	7.3
CA	750	51.4	0.2	2.9	6.4	39.1	17.2	32.4
ND (2 step)	350	59.6	3.7	2.9	16.8	16.8	39.9	6.3
ND (2 step)	450	62.7	2.6	3	12.9	12.9	35	7.8
ND (2 step)	550	63.9	1.8	5	8.2	8.2	33.2	12.3
ND (2 step)	650	63.3	0.9	8.6	5.6	5.6	31.1	43.6
ND (2 step)	750	60.3	0.7	8.7	1.2	1.3	27	63.1
ND (1 step)	750	46.7	0.6	16	4.30	4.3	22.7	110.3

Nitrogen-doped chars were successfully applied to capture phosphate from the aqueous phase. Chars derived from AD fiber after N-doping exhibited excellent properties in terms of composition, porous structure, and functional groups, and displayed favorable potential adsorption properties for phosphate from aqueous solution compared to CO₂-activated char. In this study, ammonia modified the property of the char and acted as a nitrogen source and pore-creating agent. Nitrogen doping altered the N configuration in the char surface and resulted in greater phosphate adsorption. The results show that production temperature plays an important role on the capacity of the resulting char towards phosphate adsorption. The maximum phosphate adsorption of the N-doped char was greater than 63 mg g⁻¹ indicating that N-doping can be an appropriate treatment for to improve the phosphate adsorption of char. When the whole process was carried out under ammonia, the adsorption capacity increased dramatically (110 mg g⁻¹), indicating that there is a link between nitrogen content and phosphate adsorption capacity.

2.3.2 Thermodynamic stability of nitrogen functionalities.

The isolated nitrogen dopants on the hydrogen-edge graphene model, all tested structures are shown in Figure 18. The types of structures tested here are monomerized pyridinic nitrogen

(P₆N-Edge), monomerized pyrrolic nitrogen (P₅NH-Edge), monomerized pyrrolic nitrogen without hydrogen (P₅N-Edge), graphitic nitrogen at the edge (GN-Edge), and a graphitic nitrogen in the ribbon center (GN-Center). According to the DFT reactions energies, P₅NH-Edge ($E_{\text{rxn}} = -0.46$ eV), GN-Edge ($E_{\text{rxn}} = 0.02$ eV), and P₆N-Edge ($E_{\text{rxn}} = 0.07$ eV) are the most favorable nitrogen defect structures. Notably, the DFT energies show that the formation of nitrogen functional groups is much more favorable at the edge of the hydrogen model than in the pristine graphene sheet. This is consistent with experiments that show nitrogen incorporation at the edges of graphene nanoribbons and n-type material upon ammonia exposure under high temperatures (Wang et al., 2009).

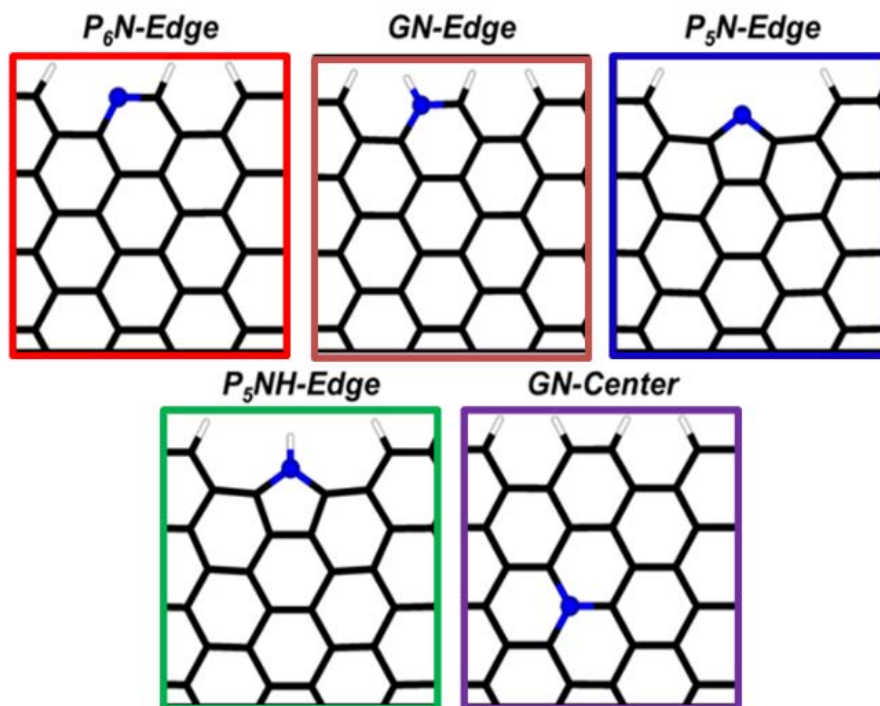


Figure 18: Top views of nitrogenated defects on the hydrogen-edge graphene model. Top panel shows isolated nitrogen defects (1 nitrogen/20 edge carbon atoms). Species are monomerized pyridinic edge (P₆N-Edge), graphitic nitrogen at the edge (GN-Edge), monomerized pyrrolic without H (P₅N-Edge), monomerized pyrrolic with H (P₅NH-Edge), and graphitic nitrogen at the center (GN-Center).

The effect of temperature and pressure on the thermodynamic stability of the different isolated nitrogen edge defects is shown in Figure 19. The formation of several of the nitrogen defects on a hydrogen terminated graphene edge are exergonic. As shown in Figure 19A, the temperature effects at 1 bar show that P₆N-Edge is the most stable defect structure over the entire temperature range, followed by the non-defect hydrogen-edge graphene and P₅NH-Edge. Finally, a comparison between the GN-Edge and GN-Center results show that, over the entire temperature and pressure range studied, nitrogen substitution is more favorable on the edge of graphene than in the center by ~ 0.5 eV

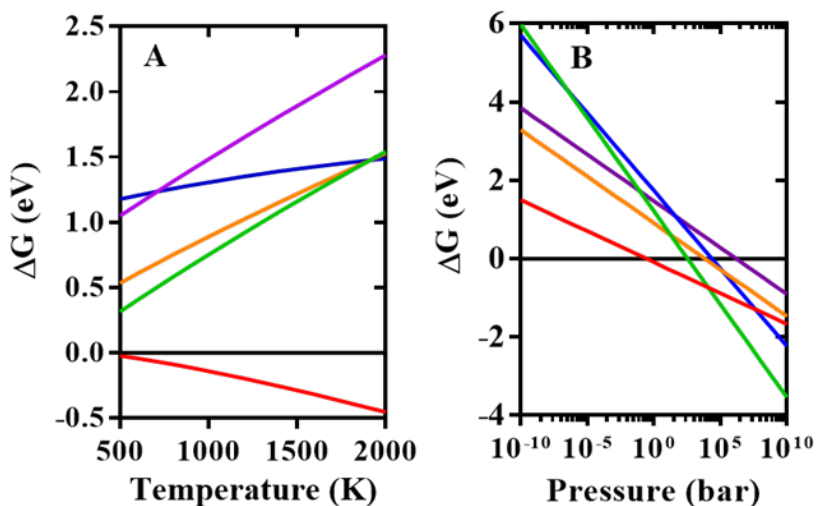


Figure 19: Phase diagram of isolated nitrogen functional groups on the hydrogen-edge graphene model with respect to (A) temperature at 1 bar and (B) pressure at 800 K. The perfect hydrogen-edge graphene sheet is the reference structure at $\Delta G = 0$ eV in both graphs.

Nitrogen functionalization of biochar significantly enhances the physical and chemical properties of these materials, increasing their applicability as sorbents, heterogeneous catalysts, and electronic components. Being able to selectively induce different nitrogen functionalities via treatment conditions is key to the design and optimization of such materials. Here, we use density functional theory to study the thermodynamic stability of nitrogen functionalities in three graphene structures as a function of temperature and pressure, providing atomistic insight into the most favorable functionalized configurations. Phase diagrams show that nitrogen incorporation is most exergonic at graphene edges, with pyridinic groups dominating under the majority of conditions studied. For all nitrogen functionalities, lower temperatures and higher pressures result in the greater incorporation of nitrogen into the graphene structures.

2.3.3 Production and characterization of N-doped char from cellulose

There is a growing interest in the production of N-doped carbonaceous materials because of their excellent properties in a variety of applications such carbon electrodes (Wang et al., 2009), heterogeneous catalysis (Cheng et al., 2019; Deng et al., 2011; Geng et al., 2011; Jafri et al., 2010; Lee et al., 2011; Lefèvre et al., 2009; Lu et al., 2009; Ozaki, 2006; Proietti et al., 2011; Wu et al., 2011; Yu et al., 2010; Zhang et al., 2006), adsorption (Adib et al., 2000; Ayiania et al., 2019a; Chen et al., 2013a; Nandi et al., 2012; Yao et al., 2013a; Yao et al., 2013b; Yao et al., 2012; Zhang et al., 2013b; Zhang et al., 2012b), and batteries (Alfarra et al., 2002; Chen et al., 2013b; Frackowiak & Beguin, 2002; Li et al., 2011; Sahu et al., 2015; Shao et al., 2010; Zhang et al., 2012a). Nitrogen is typically introduced into chars in two ways: (1) carbonizing nitrogen-containing organic compounds (*e.g.*, melamine (Lai et al., 2012; Sheng et al., 2011; Wang et al., 2013), 3-methyl-1-butylpyridine dicyanamide ionic liquid (Byambasuren et al., 2016; Liu et al., 2013)), or (2) treating a carbonaceous material at high temperatures with nitrogen-containing gases which decompose at reactor temperatures, generating highly reactive radicals (for example,

using ammonia gas (Chen et al., 2016; Luo et al., 2014; Mangun et al., 2001; Wang et al., 2009)). These radicals react with the carbonaceous material to form pyridines, pyrroles, graphitic nitrogen, amines, pyridones, and N-oxides. Nitrogen-containing functionalities are responsible for an increase in the surface polarity of carbons (Lahaye et al., 1999), and for basicity, since both pyridines and pyrrole-type structures are considered basic (Lahaye et al., 1999). However, in general, the acidic/basic character is governed by the heterogeneity of the nitrogen containing surface groups (El-Sayed & Bandosz, 2002) and also the nitrogen group in the structure of biochar changes the structural configuration and hence create more active sites for potential binding to pollutants

Lignocellulosic materials (e.g., wheat straw, AD fiber) contain cellulose, hemicellulose, lignin and ash. In order to isolate the effect of the hemicellulose and lignin as found in lignocellulosic material on phosphate adsorption, it is helpful to use pure cellulose to better understand what is responsible for phosphate adsorption. In this research, five samples of N-doped chars were produced via pyrolyzing/carbonizing cellulose under ammonia gas at different temperatures (500, 600, 700, 800, 850 and 900°C) in order to find the optimum temperature of maximum nitrogen incorporation in the structure of biochar. This is similar to the 'one step' N-doping described in Figure 11, but at a range of temperatures and with cellulose as a feedstock.

The following analytical techniques were used for the biochar characterization: elemental and proximate analysis, gas physisorption analysis. Characterization of the resulting chars shows an increase of the nitrogen content in the samples, where the greatest nitrogen content appears at a temperature of 800°C (12.5 wt. %) (Table 5). High surface area was achieved through ammonia doping of cellulose char with ammonia serving as an activating agent. The surface area analysis shows an increase in surface area of the biochar as the production temperatures increase (500-900°C). The adsorption isotherm for the surface analysis test are shown in Figure 20. Note that specific surface area and pore volume are commonly determined by measurement of physisorption of N₂ and/or CO₂. The maximum surface area (1314 m² g⁻¹, see Table 6) was achieved at 900°C. It is worth mentioning that high surface area and pore volume are key biochar properties that are related to water and nutrient cycling, microbial activity as well as sorption potential for organic and inorganic compounds as well as gaseous pollutants.

Table 5: Elemental content of N-doped chars from cellulose.

Samples	Dry basis			
	C (wt.%)	H (wt. %)	N (wt. %)	O (wt. %)
N-dopedchar_500	86.6	3.1	7.4	2.9
N-dopedchar_600	87.5	2.2	7.8	2.6
N-dopedchar_700	85.4	1.2	11.0	2.4
N-dopedchar_800	84.7	0.9	12.5	1.9
N-dopedchar_900	89.6	0.6	7.6	2.1

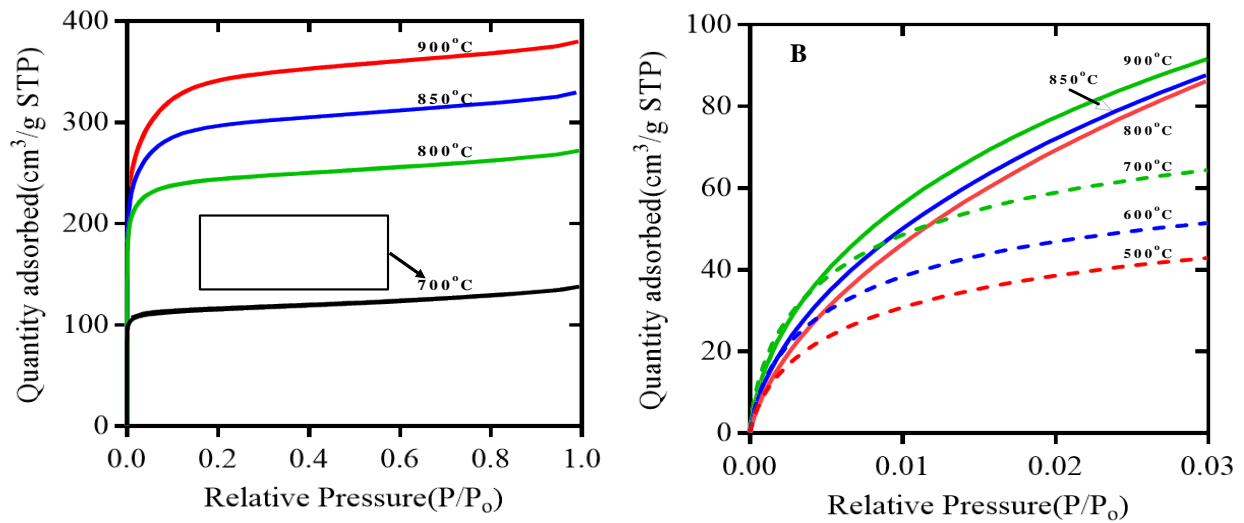


Figure 20: Adsorption isotherms of nitrogen-doped chars produced from cellulose. (A) is N_2 adsorption isotherm and (B) is CO_2 adsorption isotherm

Table 6: Surface area (Sa) and pore volume (PV) of N-doped chars from cellulose.

Sample	Sa _{N₂} (m ² g ⁻¹)	SaCO ₂ (m ² g ⁻¹)	PV _{micro} (cm ³ g ⁻¹)	PV _{meso} (cm ³ g ⁻¹)	PV _{total} (cm ³ g ⁻¹)
N-dopedchar_500	-	331.7	0.13	-	-
N-dopedchar_600	-	386.2	0.15	-	-
N-dopedchar_700	453.2	470.9	0.19	0.02	0.21
N-dopedchar_800	934.1	761.0	0.30	0.12	0.42
N-dopedchar_850	1169.9	764.2	0.31	0.20	0.51
N-dopedchar_900	1314.8	793.4	0.32	0.27	0.59

2.3.4 Effect of N-doping on water holding capacity

In this part of the project, biochar with and without nitrogen doping was produced from two fractions of municipal solid waste: particle board (Recovery 1 Inc., Tacoma, Washington) and compost overs (Royal Organics, Royal City, Washington) using a two-step process (first step is pyrolysis under N₂ and second step is ammonization under ammonia gas). These materials were chosen for this test because they are part of the municipal solid waste fractions and their heavy metal content is among the lowest of the municipal solid waste fractions tested in a previous study (Ayania et al., 2019). The characteristics of these materials are shown in Table 7 and Table 8. The water holding capacity (WHC) of soil and biochar mixtures are shown in Figure 21 and Table 9. The biochar produced was mixed with sandy soil at 2, 5, and 10 wt. %. The results show that adding biochar to sandy soil significantly increases the WHC and that WHC increases with the amount of biochar added. However, an interesting point observed is that in the cases of particle board at 5 and 10 wt. %, and compost overs at 10 wt. % mixing rates, the N-doped biochar had less water holding capacity when compared to the undoped biochar. One of the most important parameters influencing WHC of biochar is the presence of oxygen functional groups. It has been proposed in the literature that during the formation of the N-doped biochar, the ammonia reacts with the oxygen functional groups on the biomass during the carbonization process under NH₃, reducing the amount of oxygen groups in the final biochar product. Hence, fewer oxygen functional groups are available to form hydrogen bonds with water molecules compared to biochar that has been produced by normal pyrolysis under N₂.

Dugan et al. blended three soils from Ghana with three different biochars at rates of 5, 10 and 15 t/ha. Maize Stover biochar mixed with soil E (loamy sand) increased WHC up to 18% at rate of 5 and 10 t/ha, for soil A (sandy loam) up to 10% at the same rates and for soil K (silt loam) up to 12%. In the case of soils mixed at rate of 15 t/ha, the WHC increased up to 12%, 7%, and 7% for Soil E, A and K respectively. The second biochar used was sawdust biochar, this increased the WHC for the three soil in values around 12% for Soil E, 8% for soil A, and 9% for soil K at the

rate of 5, 10 and 15 t/ha. Lastly, charcoal mixed with soil E at three different rates did not show any variation in the WHC content compared to the WHC for the soil alone. Soil A, at the same rates retained up to 10% in WHC and for Soil K at rate of 5t/ha the WHC increased up to 18%, and 15% of WHC for 10 and 15 t/ha, respectively.

In Yu et al. (2013) work, soil (loamy sand) was blended with untreated yellow pine scrap lumber biochar at different rates from 1 to 10 wt. %. Adding 2 wt. % of this biochar to soil showed an increase of WHC content up to 3%. For 5 wt. % of biochar WHC increased up to 7.5% and for 10 wt.% biochar increased the WHC up to 16.3%.

In our research, the WHC increased up to 3.1% when Quincy sand soil was mixed with 2 wt. % of particle board (PB) and compost overs (CO) raw biochar. At mixing rate of 5 wt. % the WHC content increased up to 20.7% for particle board biochar and 11.1% for compost over biochar. 10 wt. % of biochar blended with soil increased WHC up to 39.7% and for CO up to 27.9%, for PB and CO, respectively. With N-doped biochar, mixing PB-N-doped char at rates of 2, 5, and 10 wt. %, the WHC content increased up to 4.7%, 16.8% and 26.9%, respectively. Nitrogen-doped char from CO, mixed at the same rates, raised WHC values up to 7.9%, 14.5% and 14.8%, respectively.

We can conclude that improvement of WHC in this study was greater than results of other studies presented above. Is very important select biochar with high surface area, to have the presence of surface functional groups, and adequate porosity structure. These are the primary factors to consider when selecting a biochar to use for improvement of soil WHC.

Table 7: Elemental analysis of municipal solid waste fractions

Samples	On dry basis (wt.%)											
	400°C				500°C				600°C			
	C	H	N	O*	C	H	N	O*	C	H	N	O*
Compost overs	76.8	3.3	1.0	12.5	79.9	2.7	1.4	8.9	83.8	1.2	1.0	6.0
Particle board	82.3	4.0	1.1	11.1	84.4	3.3	1.6	10.3	90.50	1.69	1.32	5.01

*Obtain by difference

Table 8: Proximate analysis of municipal solid waste fractions including moisture content (M wt. %), volatile carbon (VC), fixed carbon (FC), and ash.

Samples	On dry basis (wt. %)											
	400°C				500°C				600°C			
	M wt.%	VC	FC	Ash	M Wt.%	VC	FC	Ash	M wt.%	VC	FC	Ash
Compost overs	2.3	21.9	71.7	6.4	3.5	16.2	76.6	7.2	3.6	9.4	82.6	7.9
Particle board	1.6	32.6	67.1	0.4	1.4	24.5	75.0	0.41	1.1	12.7	86.7	0.5

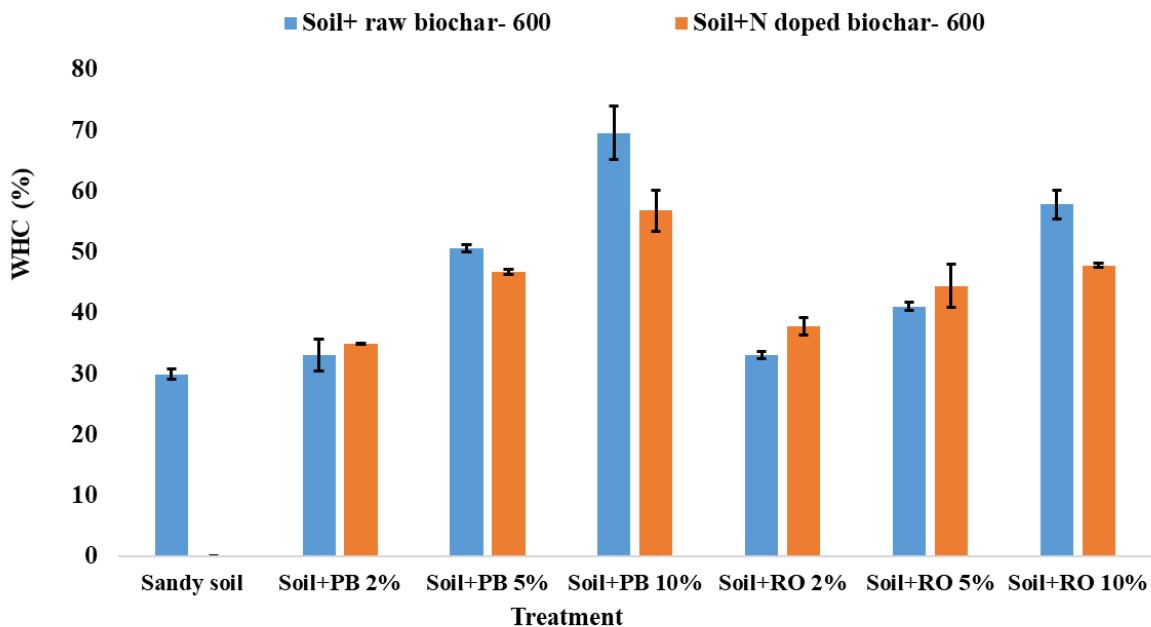


Figure 21: Effect of addition of raw and N-doped biochar at 2, 5, and 10 wt. % on water holding capacity (WHC) of Quincy sand. PB = particle board feedstock, CO = compost overs feedstock.

Table 9: Effect of biochar from particle board (PB) and compost overs (CO) on water holding capacity (WHC) of sandy soil.

Sample Name	WHC (%)
Sandy soil	29.9±0.84
Soil+PB 2%	33.0±2.64
Soil+PB-N 2%	34.9±0.09
Soil PB 5%	50.6±0.58
Soil+PB-N 5%	46.7±0.49
Soil+PB 10%	69.6±4.32
Soil+PB-N 10%	56.8±3.34
Soil+CO 2%	33.0±0.63
Soil+CO-N 2%	37.8±1.42
Soil+CO 5%	41.0±0.63
Soil+CO-N 5%	44.4±3.53
Soil+CO 10%	57.8±2.39
Soil+CO-N 10%	44.7±0.34

2.4 Conclusions

The first part of this chapter described the use of anaerobically digested fiber to engineer a biochar with nitrogen capable of retaining phosphate. This concept was proposed to make use of the fiber after anaerobic digestion to remove phosphate from AD effluent. We found that biochar with high ash content doped with nitrogen in a two-step process is very effective in nutrient recovery (63.1 mg g^{-1}). However, using the one step process led to a two-fold increase in the nitrogen content in the structure of the biochar, doubling the phosphate adsorption capacity of the biochar (110.3 mg g^{-1}). In the second part of this chapter involved the use of molecular modeling tools to evaluate the stability of different functional groups present in char. This study showed that pyridine is the most stable functional group for all ranges of temperatures. Overall, this work allows for the identification of temperature and pressure combinations that can be adjusted to affect the distribution of nitrogen functional groups in carbonaceous materials during the heat treatment nitrogen doping process with potential applications in the areas of filtrant design, heterogeneous catalysis, adsorbents and electronics. The third part was to study the production and characterization of nitrogen-doped char from cellulose at different temperatures. The maximum nitrogen content (12.5 wt. %) was incorporated in the char at a temperature of 800°C and the highest surface area was obtained ($1315 \text{ m}^2 \text{ g}^{-1}$) at 900°C . This study provides the optimum temperature at which we can get maximum incorporation of nitrogen in the biochar structure. Lastly, biochar produced from particle board and compost overs with and without nitrogen doping were used to evaluate the water holding capacity of the biochar. Our results show that biochar mixed with sandy soil increased water holding capacity compared to sandy soil alone. Interestingly, N-doping reduced the biochar's water holding capacity at higher application rates.

3. Third Generation Biochars: Nitrogen-Metal Doping

3.1 Introduction

This chapter explores the synergistic effect between metals and nitrogen in biochar in the removal of phosphate ions. Our previous experience in phosphate retention using AD fiber was discussed in Chapter 2. In this work we found that more phosphate is been retained on biochar when both ash and nitrogen content are present in the biochar. We carried out an inductively coupled plasma mass spectroscopy (ICPMS) analysis to determine the content of the metals present in AD fiber biochar. We notice that the most prominent metals were Ca, Mg, and Fe. Other studies in the literature also used Ca and Mg impregnated biomass and the resulting biochar presented a high capacity to retain phosphate (Yao et al., 2013b; Yao et al., 2011a). Based on these experiences, we wanted to have a clear understanding of which metals in the ash, combine with nitrogen, are responsible for the efficient removal of phosphate ions from aqueous solutions. In order to isolate the effect of the rest of the components of lignocellulosic materials (cellulose, hemicellulose, lignin and ash). We used pure cellulose as the base feedstock. The three most prominent metals found in AD fiber were impregnated individually in cellulose. The objective of this work is to develop design guidelines for biochar production with excellent properties for phosphate retention. This part of the project evaluates the synergistic effect between nitrogen functionalities and different metals content on the removal of phosphate ions.

3.2 Methods

3.2.1 Nitrogen metal-doped biochar production

In order to isolate the effect of the other components of the lignocellulosic materials, only cellulose material was used. A solution of Mg, Ca and Fe was prepared and later mixed with powdered cellulose (Figure 22). The mixture was then oven dried for 24 hours. In order to achieve maximum nitrogen incorporation in the structure of biochar, a one-step carbonization process was carried out under ammonia in a Quartz Tube furnace reactor with 50 mm OD by 44 mm ID at a length of 1000 mm at 800°C, as described in Section 2.2.1 of this report. The resulting char doped with nitrogen and metals was then characterized and used for phosphate retention studies, using the methods outlined in Section 2.2.2. Note that this same method was used for wheat straw.

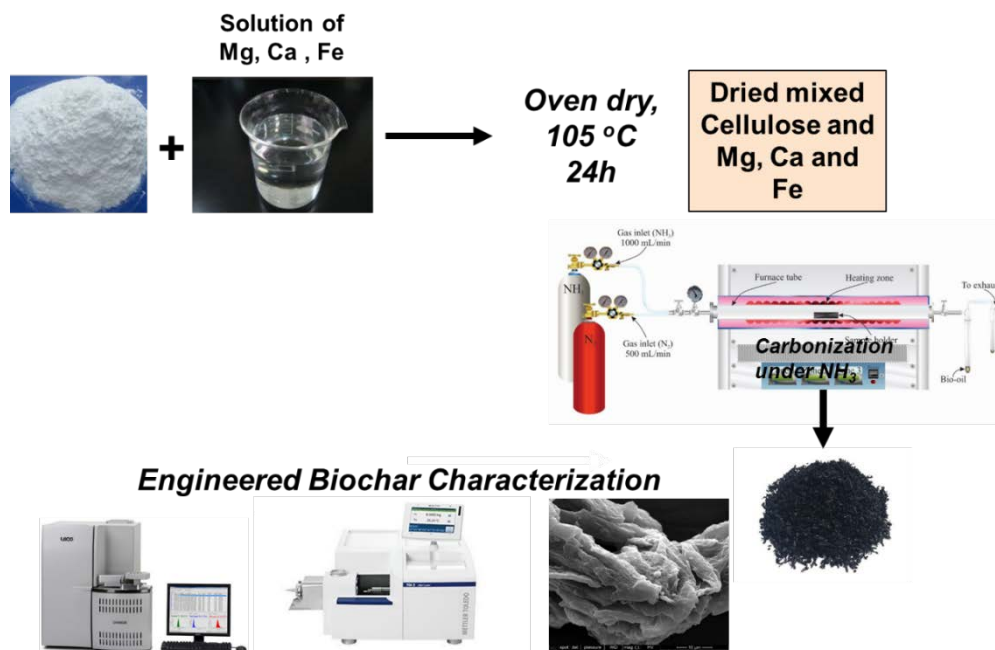


Figure 22: Method used for the production of metal-N-doped chars.

3.2.2 X-ray photoelectron spectroscopy

Analysis using XPS was performed using an AXIS-165 upgraded to an Ultra manufactured by Kratos Analytical Inc. Achromatic X-ray radiation of 1253.6 eV ($MgK\alpha$) was used to analyze each material. All high-resolution spectra were recorded using a pass energy of 40 eV and spot size of approximately 120 μm . The spectrometer was calibrated against both the Au $4f_{7/2}$ peak at 84.0 eV and the Ag $3d_{5/2}$ peak at 368.3 eV. The minimum full width at half maximum (FWHM) for the Au $4f_{7/2}$ peak is approximately 0.85 eV, representing the absolute minimum possible broadness achievable for this configuration. Survey scans have been obtained using a pass energy of 80 eV and step sizes of 1 eV to determine the overall chemical composition of each sample. To determine the speciation of carbon, nitrogen and oxygen groups, high resolution scans of the C 1s, N 1s, O 1s and Mg 2p regions (280-295, 394-404, 527-538 eV, 45-60 eV respectively) were collected for each material using 0.1 eV step sizes.

3.2.3 Elemental analysis

Elemental analysis was performed using a TRUSPEC-CHN[®] elemental analyzer (LECO, U.S.) (Ayiania et al., 2019b). Briefly, 0.15 g of sample was used to determine total carbon (C), nitrogen (N) and hydrogen (H) contents. Oxygen (O) mass fraction was determined by subtracting the ash, C, N, and H contents from the total mass of the sample.

3.3 Results and Discussion

3.3.1 Biochar from metal and N-doped cellulose

The elemental and proximate analysis of char doped with metals and nitrogen is presented in Table 10. The presence of metals had a significant influence on the carbonization process. More nitrogen is being incorporated in the structure of the char, particularly for the Mg-N-char, which has 15.5 wt. % nitrogen compared to 12.5 wt. % nitrogen for the N-doped char (Table 10). However, the carbon content decreases dramatically as compared to char without metals. While the reason for the decrease in carbon content is not entirely clear, it's possible that the metals may have had a catalytic effect during the carbonization process.

Table 10: Elemental composition of metal-N-doped char derived from cellulose

Samples	Dry basis						
	C (wt.%)	H (wt. %)	N (wt. %)	O (wt. %)	VC (wt. %)	FC (wt.%)	Ash (wt. %)
N-dopedchar_800 °C	84.7	0.9	12.5	1.9	10.2	89.8	0.0
Mg-dopedchar_800 °C	65.8	0.8	0.2	5.1	4.4	67.5	28.1
Mg-N-dopedchar_800 °C	51.5	1.0	15.5	7.8	14.7	61.0	24.2
Ca-N-dopedchar_800 °C	62.1	0.6	12.9	0.7	11.6	64.5	23.9
Fe-N-dopedchar_800 °C	69.0	0.8	8.8	2.8	13.6	67.8	18.6

X-ray photoelectron spectroscopy was conducted to see the elements on the surface of the char and understand the bonding patterns. XPS is a spectroscopy technique to determine the elemental composition on the surface of the biochar. The X-rays can penetrate up to a depth of 10 nm. The surface elements present in each biochar are shown in Figure 23. To determine the speciation of carbon, nitrogen oxygen and magnesium groups, high resolution scans of the C 1s, N 1s O 1s and Mg 2p regions (280-295, 394-404 ,527-538 eV, 45-60 eV respectively) were collected for each material using 0.1 eV step size.

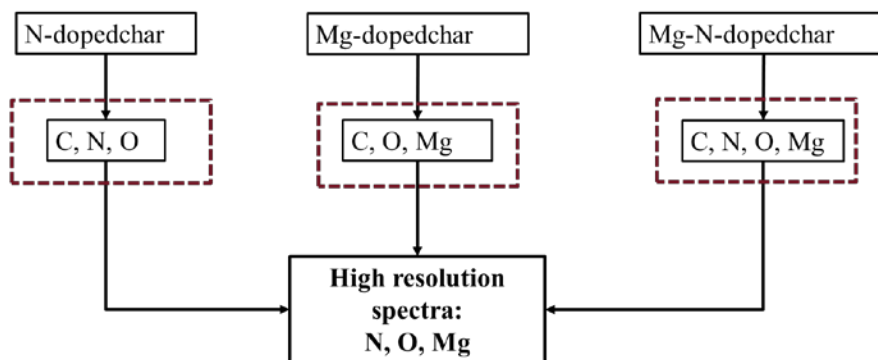


Figure 23: Surface elemental composition on N-doped char (char doped with only nitrogen), Mg-doped char (char impregnated with magnesium), and Mg-N-doped char (char with both magnesium and nitrogen).

The high-resolution spectra taken for each of the biochars are shown in Figure 24. The spectra provide useful information on the bonding pattern for the different elements present in the biochar. Figure 24A shows the spectra of nitrogen. Notice that for the spectra of Char_N (only nitrogen doping) and Char_Mg_N (impregnated with magnesium and N-doped) both present two prominent peaks at a binding energy of 398.8 eV and 401.5 eV. These peaks correspond to pyridinic and pyrrolic nitrogen respectively (Figure 25). However, it can be observed that the intensity of the spectra for char_Mg_N at 401.5eV decreased compared the Char_N. These changes noticed might be suggesting that the magnesium in the biochar might be forming a bond with the nitrogen in the pyrrolic group.

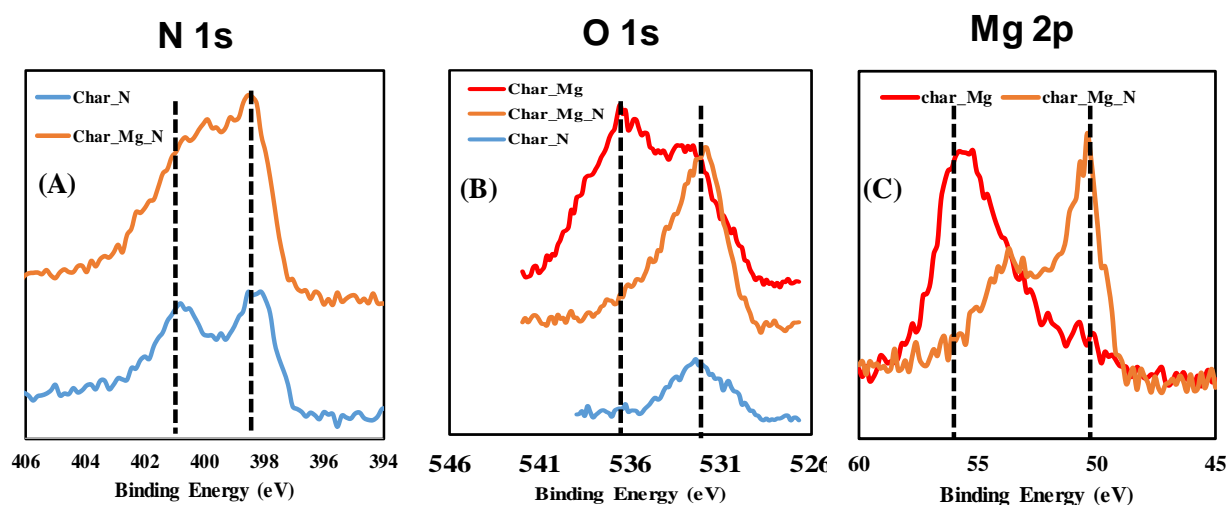


Figure 24: XPS spectra of N-doped char and Mg-N-doped char. Figure A is the N 1s spectra where each peak is a different configuration if nitrogen. Figure B is the O 1S where each peak is a different type of oxygen bonding. Figure C is different types of Mg bonding with oxygen, nitrogen and carbon.

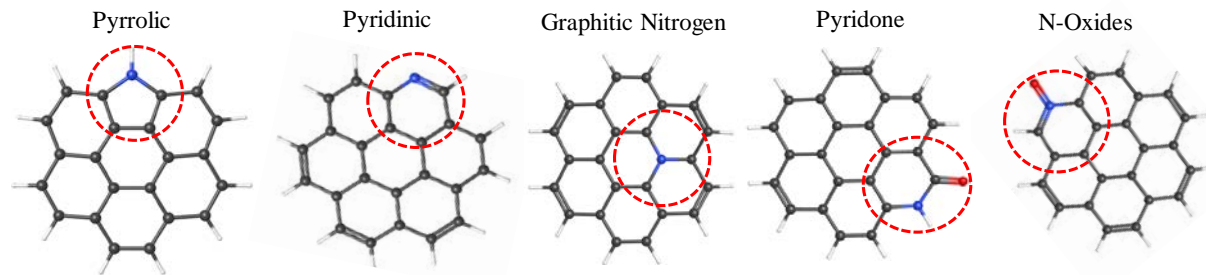


Figure 25: Structural configurations of individually different types of nitrogen within a coronene model structure. where pyrrolic (edge nitrogen within a five-member ring), pyridinic (edge nitrogen within a six-member ring), graphitic (direct substitution of a carbon atom within a graphite plane), pyridone (edge nitrogen within a six-member ring with one carbon double bonded to oxygen) and N-oxides(edge oxygen double bonded to nitrogen within a six-member ring)

Figure 24B shows how the oxygen is bonded in the structure of biochar. We observed something very interesting in the spectra. A partially symmetric spectra with an optimum binding energy of 531.8 eV is observed for Char_N and Char_Mg_N. However, looking at the Char_Mg (char impregnated with magnesium and without nitrogen), two prominent peaks are observed and are situated at 531.8 eV and 536.5 eV. The peak at 536.5 eV is linked to Magnesium Oxides (MgO). It is important to mention that when both Mg and N (Char_Mg_N) are present in the biochar the peak at 536.5 is not observed. With this observation we are hypothesizing that in the presence of nitrogen the metal (magnesium) prefer to bind to nitrogen over oxygen.

To further confirm our hypothesis, we analyzed the magnesium spectra (Mg 2p) shown in Figure 24C. Obviously, one prominent peak in seem for Char_Mg situated at 56.2 eV. However, for Char_Mg_N two peak are observed with the peak at 50.2 eV being the most prominent and might be related to a bond formation between magnesium and nitrogen. This details analysis of the high-resolution spectra shows that the magnesium in the char prefers to bond with nitrogen over oxygen. This bonding pattern can be seen in Figure 26.

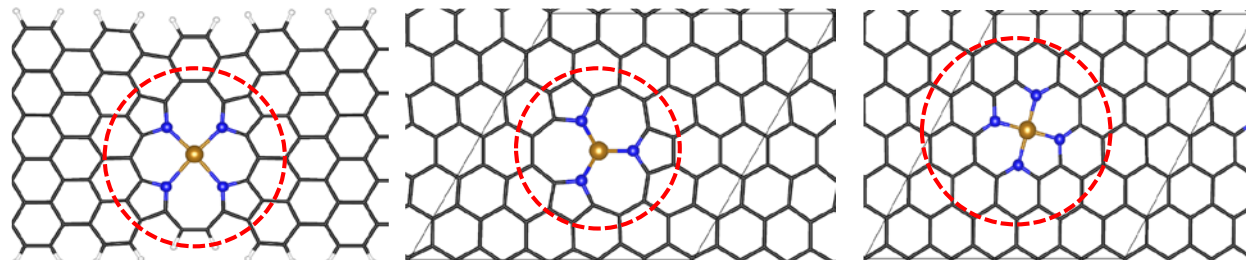


Figure 26: Molecular scheme of Mg-N-doped chars within a graphene model structure. Where the first structure is Mg bonded to 4-N within a pyrrolic group. Middle structure is Mg bonded to 3-N within a pyrrolic group and the last structure is Mg bonded to 4-N within a pyridine group.

The chars containing metals and nitrogen were tested for phosphate adsorption capacity. The results demonstrate that Mg-N- and Ca-N-doped char had excellent phosphate adsorption

capacity (335mg g^{-1} and 178 mg g^{-1} , respectively; Figure 27). However, Fe- N-doped char had poor capacity for adsorption of phosphate ions. Interestingly, chars with N or Mg alone, did not have nearly the phosphate adsorption capacity of the Mg-N-doped chars, suggesting a synergistic effect between metals (specifically, Mg and Ca) and N on the phosphate removal. Figure 28 shows the tubes with phosphate solution after 24 hours of contact with char; the yellow color is directly proportional to the concentration of phosphate. This provides a visual representation of the effectiveness of Mg-N-char as compared to chars with Mg or N, alone.

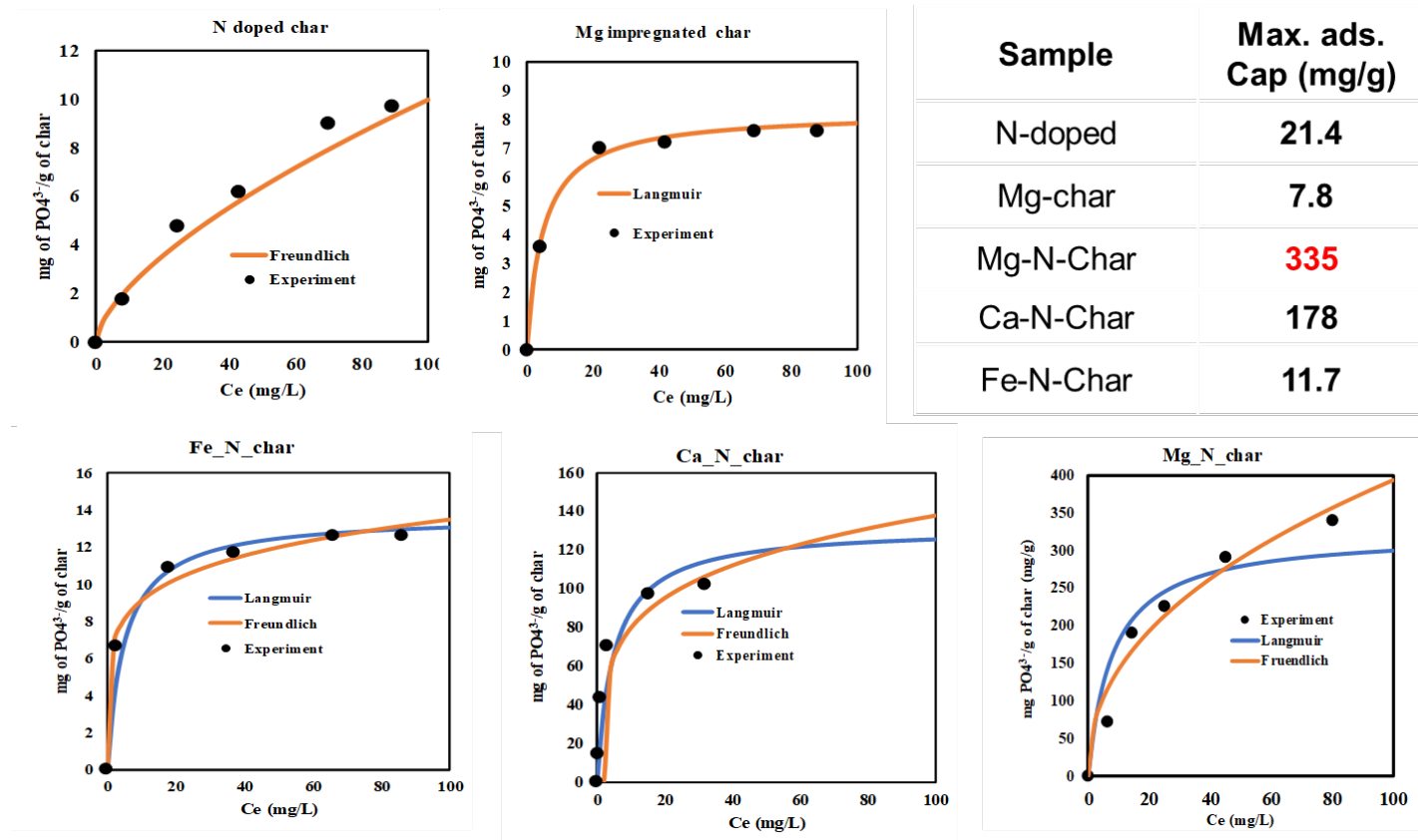


Figure 27: Phosphorus Adsorption Isotherm of metal-N-doped chars derived from cellulose.

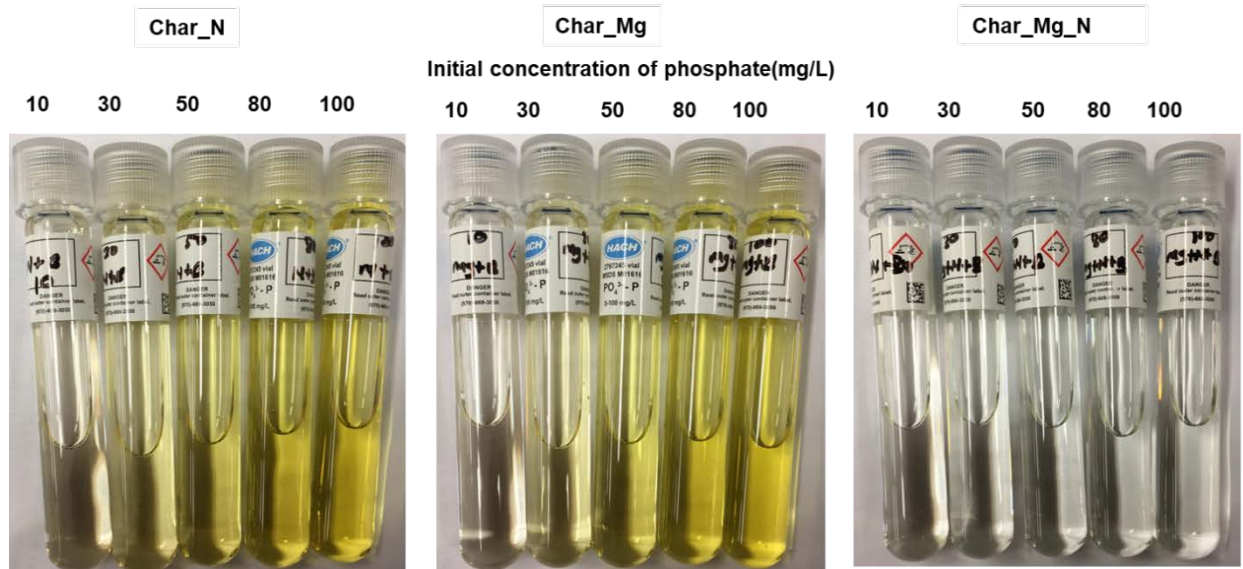


Figure 28: Phosphate adsorption by metal and N-doped biochar derived from cellulose (pyrolyzed at 800°C) from solutions of varying initial concentrations. The color intensity is directly proportional to the remaining concentration of phosphate after treatment with biochar for 24 hours, with more intense yellow indicating higher concentrations of phosphate. The photo on the left shows phosphate concentration after being in contact with N-doped biochar (Char_N). The photo in the middle shows solutions that have been in contact with Mg-doped biochar (Char_Mg). The photo on the right shows solutions after contact with Mg-N-doped biochar (Char_Mg_N). The fact that all test tubes are colorless on the right indicates that this biochar has been very effective at removing phosphate ions.

3.3.2 Biochar from metal and N-doped wheat straw

We further tested the effectiveness of Mg-N-doped chars by using a lignocellulosic material - wheat straw. The material was impregnated with magnesium and later doped with N. The resulting char showed very high phosphate adsorption capacity (288 mg g^{-1}) compared to the same material without Mg-N-doping (60 mg g^{-1} ; Figure 29). The corresponding adsorption capacities are shown in Table 11

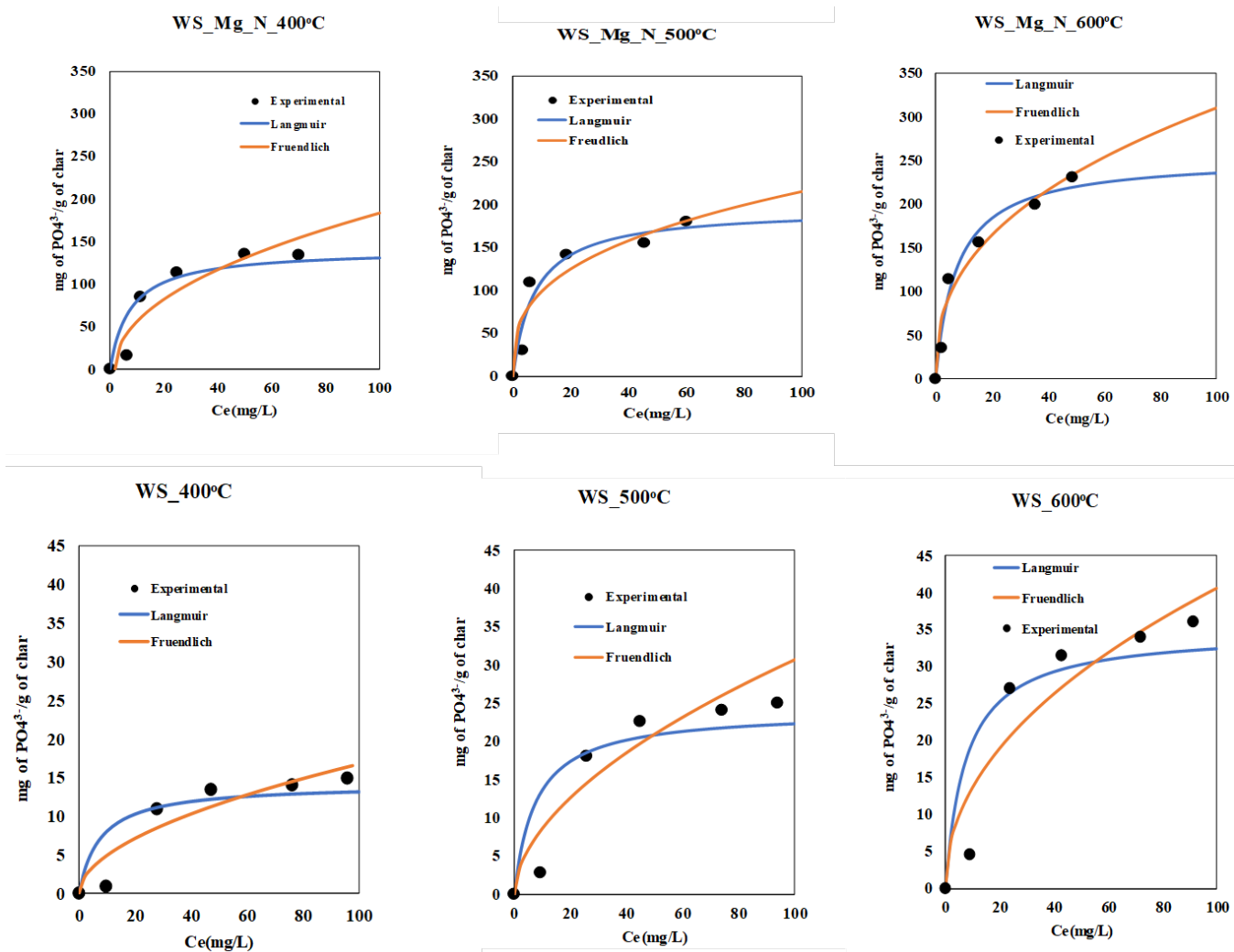


Figure 29: Phosphorus adsorption isotherms of Mg-N-doped chars derived from wheat straw

Table 11: Result of phosphate adsorption capacity of wheat straw biochar

Samples	Biochar Production Temp. (°C)	Max. adsorption capacity of char towards phosphate (mg g ⁻¹)
Wheat straw	400	18.8
Wheat straw	500	30.8
Wheat straw	600	60.1
Wheat Straw Mg-N	400	136.2
Wheat Straw Mg-N	500	194.8
Wheat Straw Mg-N	600	288.4

3.4 Conclusions

We have evaluated the effect of different metals and nitrogen on the capacity of biochar to adsorb phosphate. We found that there is a synergistic effect between Mg and Ca with N-doped char, with the Mg-N- and Ca-N-doped chars providing substantially improved capacity to remove phosphate ions. In this report we have shown that Mg and Ca are very important metals to consider when designing adsorbent for phosphate retention. However, these metals do not possess the complete capacity in biochar to retain phosphate ions without nitrogen in the structure of biochar. Hence, with the results obtained in this chapter we lay out fundamental guidelines to design phosphate retention adsorbents from any feedstock

Technically, since these biochars have excellent capacity to retain nutrients, they could be used for soil amendment. However, biochar for soil amendment should have the capacity to slowly release the nutrients to plants (i.e., the nutrient should be bioavailable to plants). Future work will involve the study of the desorption process to get a mechanistic understanding of how strongly the nutrients are bonded to the biochar, affecting their bioavailability to plants.

4. References

- Adib, F., Bagreev, A., Bandosz, T.J. 2000. Adsorption/oxidation of hydrogen sulfide on nitrogen-containing activated carbons. *Langmuir*, 16(4), 1980-1986.
- Agvise Laboratories, n.d. Water Holding Capacity: <https://www.agvise.com/educational-articles/water-holding-capacity/>. Accessed 10 June 2019.
- Alfarra, A., Frackowiak, E., Béguin, F. 2002. Mechanism of lithium electrosorption by activated carbons. *Electrochimica Acta*, 47(10), 1545-1553.
- Antunes, E., Jacob, M.V., Brodie, G., Schneider, P.A. 2018. Isotherms, kinetics and mechanism analysis of phosphorus recovery from aqueous solution by calcium-rich biochar produced from biosolids via microwave pyrolysis. *Journal of Environmental Chemical Engineering*, 6(1), 395-403.
- Arenas-Lago, D., Vega, F., Silva, L., Andrade, M. 2013. Soil interaction and fractionation of added cadmium in some Galician soils. *Microchemical Journal*, 110, 681-690.
- Ayiania, M., Carbajal-Gamarra, F.M., Garcia-Perez, T., Frear, C., Suliman, W., Garcia-Perez, M. 2019a. Production and characterization of H₂S and PO₄³⁻ carbonaceous adsorbents from anaerobic digested fibers. *Biomass and Bioenergy*, 120, 339-349.
- Ayiania, M., Terrell, E., Dunsmoor, A., Carbajal-Gamarra, F.M., Garcia-Perez, M. 2019b. Characterization of solid and vapor products from thermochemical conversion of municipal solid waste woody fractions. *Waste Management*, 84, 277-285.
- Babel, S., Kurniawan, T.A. 2004. Cr (VI) removal from synthetic wastewater using coconut shell charcoal and commercial activated carbon modified with oxidizing agents and/or chitosan. *Chemosphere*, 54(7), 951-967.
- Bagreev, A., Bandosz, T.J. 2005. On the Mechanism of Hydrogen Sulfide Removal from Moist Air on Catalytic Carbonaceous Adsorbents. *Industrial & Engineering Chemistry Research*, 44(3), 530-538.
- Ban, A., Schafer, A., Wendt, H. 1998. Fundamentals of electrosorption on activated carbon for wastewater treatment of industrial effluents. *Journal of Applied Electrochemistry*, 28(3), 227-236.
- Bandosz, T.J., Ania, C. 2006. Surface chemistry of activated carbons and its characterization. in: *Interface Science and Technology*, Vol. 7, Elsevier, pp. 159-229.
- Basso, A.S., Miguez, F.E., Laird, D.A., Horton, R., Westgate, M. 2013. Assessing potential of biochar for increasing water-holding capacity of sandy soils. *Gcb Bioenergy*, 5(2), 132-143.

- Batista, E.M., Shultz, J., Matos, T.T., Fornari, M.R., Ferreira, T.M., Szpoganicz, B., de Freitas, R.A., Mangrich, A.S. 2018. Effect of surface and porosity of biochar on water holding capacity aiming indirectly at preservation of the amazon biome. *Scientific reports*, 8(1), 10677.
- Bhatt, M.D., Lee, G., Lee, J.S. 2017. Density Functional Theory (DFT) Calculations for Oxygen Reduction Reaction Mechanisms on Metal-, Nitrogen-co-doped Graphene (M-N₂-G (M= Ti, Cu, Mo, Nb and Ru)) Electrocatalysts. *Electrochimica Acta*, 228, 619-627.
- Boehm, H.P. 1966. Chemical identification of surface groups. in: *Advances in catalysis.*, Vol. 16, Elsevier, pp. 179-274.
- Boeykens, S.P., Piol, M.N., Samudio Legal, L., Saralegui, A.B., Vázquez, C. 2017. Eutrophication decrease: Phosphate adsorption processes in presence of nitrates. *Journal of Environmental Management*, 203, 888-895.
- Břendová, K., Tlustoš, P., Száková, J., Habart, J. 2012. Biochar properties from different materials of plant origin. *European Chemical Bulletin*, 1(12), 535-539.
- Byambasuren, U., Jeon, Y., Altansukh, D., Ji, Y., Shul, Y.-G. 2016. One-step synthesis of dual-transition metal substitution on ionic liquid-based N-doped mesoporous carbon for oxygen reduction reaction. *Carbon letters*, 17(1), 53-64.
- Cantrell, K.B., Hunt, P.G., Uchimiya, M., Novak, J.M., Ro, K.S. 2012. Impact of pyrolysis temperature and manure source on physicochemical characteristics of biochar. *Bioresource technology*, 107, 419-428.
- Cao, X., Harris, W. 2010. Properties of dairy-manure-derived biochar pertinent to its potential use in remediation. *Bioresource Technology*, 101(14), 5222-5228.
- Chang, J., Ma, J., Ma, Q., Zhang, D., Qiao, N., Hu, M., Ma, H. 2016. Adsorption of methylene blue onto Fe₃O₄/activated montmorillonite nanocomposite. *Applied Clay Science*, 119, 132-140.
- Chase, M., Curnutt, J.L., Hu, A., Prophet, H., Syverud, A., Walker, L. 1974. JANAF thermochemical tables, 1974 supplement. *Journal of Physical and Chemical Reference Data*, 3(2), 311-480.
- Chen, H., Sun, F., Wang, J., Li, W., Qiao, W., Ling, L., Long, D. 2013a. Nitrogen doping effects on the physical and chemical properties of mesoporous carbons. *The Journal of Physical Chemistry. C*, 117(16), 8318-8328.
- Chen, P., Xiao, T.Y., Qian, Y.H., Li, S.S., Yu, S.H. 2013b. A Nitrogen-doped graphene/carbon nanotube nanocomposite with synergistically enhanced electrochemical activity. *Advanced Materials*, 25(23), 3192-3196.
- Chen, W., Cannon, F.S., Rangel-Mendez, J.R. 2005. Ammonia-tailoring of GAC to enhance perchlorate removal. II: Perchlorate adsorption. *Carbon*, 43(3), 581-590.

- Chen, W., Yang, H., Chen, Y., Chen, X., Fang, Y., Chen, H. 2016. Biomass pyrolysis for nitrogen-containing liquid chemicals and nitrogen-doped carbon materials. *Journal of analytical and applied pyrolysis*, 120, 186-193.
- Cheng, Y., Zhao, S., Li, H., He, S., Veder, J.-P., Johannessen, B., Xiao, J., Lu, S., Pan, J., Chisholm, M.F. 2019. Unsaturated edge-anchored Ni single atoms on porous microwave exfoliated graphene oxide for electrochemical CO₂. *Applied Catalysis. B, Environmental*, 243, 294-303.
- Chuvilin, A., Meyer, J.C., Algara-Siller, G., Kaiser, U. 2009. From graphene constrictions to single carbon chains. *New Journal of Physics*, 11(8), 083019.
- Costa, E., Sotelo, J., Calleja, G., Marron, C. 1981. Adsorption of binary and ternary hydrocarbon gas mixtures on activated carbon: experimental determination and theoretical prediction of the ternary equilibrium data. *AIChE Journal*, 27(1), 5-12.
- Cruz-Silva, E., Barnett, Z., Sumpter, B.G., Meunier, V. 2011. Structural, magnetic, and transport properties of substitutionally doped graphene nanoribbons from first principles. *Physical Review B*, 83(15), 155445.
- Chouchene, A., Jeguirim, M., Khiari, B., Trouvé, G., Zagrouba, F. 2010. Study on the emission mechanism during devolatilization/char oxidation and direct oxidation of olive solid waste in a fixed bed reactor. *Journal of analytical and applied pyrolysis*, 87(1), 168-174.
- Demirbas, A. 2004. Effects of temperature and particle size on bio-char yield from pyrolysis of agricultural residues. *Journal of analytical and applied pyrolysis*, 72(2), 243-248.
- Deng, D., Pan, X., Yu, L., Cui, Y., Jiang, Y., Qi, J., Li, W.-X., Fu, Q., Ma, X., Xue, Q. 2011. Toward N-doped graphene via solvothermal synthesis. *Chemistry of Materials*, 23(5), 1188-1193.
- Denis, P.A. 2013. Organic chemistry of graphene: the Diels–Alder reaction. *Chemistry--A European Journal*, 19(46), 15719-15725.
- Dresselhaus, M., Dresselhaus, G. 1981. Intercalation compounds of graphite. *Advances in Physics*, 30(2), 139-326.
- Dubinin, M.M., Radushkevich, L. 1947. Equation of the characteristic curve of activated charcoal. *Chem. Zentr*, 1(1), 875.
- Dubinin, M.M., Zaverina, E., Radushkevich, L. 1947. Sorption and structure of active carbons. I. Adsorption of organic vapors. *Zhurnal Fizicheskoi Khimii*, 21(3), 151-162.
- Duesberg, G., Graham, A., Kreupl, F., Liebau, M., Seidel, R., Unger, E., Hoenlein, W. 2004. Ways towards the scaleable integration of carbon nanotubes into silicon based technology. *Diamond and Related Materials*, 13(2), 354-361.

- El-Sayed, Y., Bandosz, T. 2002. An IGC and TA study of acetaldehyde adsorption on activated carbons. in: *Studies in Surface Science and Catalysis*, Vol. 144, Elsevier, pp. 247-254.
- Eriksson, O., Finnveden, G., Ekvall, T., Björklund, A. 2007. Life cycle assessment of fuels for district heating: A comparison of waste incineration, biomass-and natural gas combustion. *Energy policy*, 35(2), 1346-1362.
- Faraca, G., Boldrin, A., Damgaard, A., Astrup, T. 2017. Environmental assessment of presence of impurity materials and chemical pollutants in wood waste meant for recycling. *SETAC Europe 27th Annual Meeting*.
- Ferraz, G.P., Frear, C., Pelaez-Samaniego, M.R., Englund, K., Garcia-Perez, M. 2016. Hot Water Extraction of Anaerobic Digested Dairy Fiber for Wood Plastic Composite Manufacturing. *BioResources*, 11(4), 8139-8154.
- Foo, K., Hameed, B. 2010. Insights into the modeling of adsorption isotherm systems. *Chemical engineering journal*, 156(1), 2-10.
- Frackowiak, E., Beguin, F. 2002. Electrochemical storage of energy in carbon nanotubes and nanostructured carbons. *Carbon*, 40(10), 1775-1787.
- Freddo, A., Cai, C., Reid, B.J. 2012. Environmental contextualisation of potential toxic elements and polycyclic aromatic hydrocarbons in biochar. *Environmental pollution*, 171, 18-24.
- Fujimoto, Y., Saito, S. 2011. Formation, stabilities, and electronic properties of nitrogen defects in graphene. *Physical Review. B*, 84(24), 245446.
- Gass, M.H., Bangert, U., Bleloch, A.L., Wang, P., Nair, R.R., Geim, A. 2008. Free-standing graphene at atomic resolution. *Nature nanotechnology*, 3(11), 676.
- Geng, D., Chen, Y., Chen, Y., Li, Y., Li, R., Sun, X., Ye, S., Knights, S. 2011. High oxygen-reduction activity and durability of nitrogen-doped graphene. *Energy & Environmental Science*, 4(3), 760-764.
- Gerber, I.C., Krashennikov, A.V., Foster, A.S., Nieminen, R.M. 2010. A first-principles study on magnetic coupling between carbon adatoms on graphene. *New Journal of Physics*, 12(11), 113021.
- Giles, S.A., Yan, Y., Vlachos, D.G. 2018. Effect of Substitutionally Doped Graphene on the Activity of Metal Nanoparticle Catalysts for the Hydrogen Oxidation Reaction. *ACS Catalysis*.
- Giménez, J., Martínez, M., de Pablo, J., Rovira, M., Duro, L. 2007. Arsenic sorption onto natural hematite, magnetite, and goethite. *Journal of Hazardous Materials*, 141(3), 575-580.
- Güngör, K., Karthikeyan, K. 2008. Phosphorus forms and extractability in dairy manure: a case study for Wisconsin on-farm anaerobic digesters. *Bioresource technology*, 99(2), 425-436.

- Guo, J., Luo, Y., Lua, A.C., Chi, R.-a., Chen, Y.-l., Bao, X.-t., Xiang, S.-x. 2007. Adsorption of hydrogen sulphide (H₂S) by activated carbons derived from oil-palm shell. *Carbon*, 45(2), 330-336.
- Guo, B., Liu, Q., Chen, E., Zhu, H., Fang, L., Gong, J.R. 2010. Controllable N-doping of graphene. *Nano letters*, 10(12), 4975-4980.
- Hach, C. 2014a. Molybdovanadate with Acid Persulfate Digestion Method1 Method 10127 1.0 to 100.0 mg/L PO₄³⁻ (HR). Edition 9.
- Hach, C. 2014b. Molybdovanadate with Acid Persulfate Digestion Method1 Method 10127 547 1.0 to 100.0 mg/L PO₄³⁻ (HR). *HACH*.
- Hashimoto, A., Suenaga, K., Gloter, A., Urita, K., Iijima, S. 2004. Direct evidence for atomic defects in graphene layers. *Nature*, 430(7002), 870.
- Hensley, A.J., Zhang, J., Vinçon, I., Hernandez, X.P., Tranca, D., Seifert, G., McEwen, J.-S., Wang, Y. 2018. Mechanistic understanding of methanol carbonylation: Interfacing homogeneous and heterogeneous catalysis via carbon supported Ir La. *Journal of Catalysis*, 361, 414-422.
- Hilber, I., Blum, F., Leifeld, J., Schmidt, H.-P., Bucheli, T.D. 2012. Quantitative determination of PAHs in biochar: a prerequisite to ensure its quality and safe application. *Journal of agricultural and food chemistry*, 60(12), 3042-3050.
- Hobson, P., Feilden, N. 1982. Production and use of biogas in agriculture. *Progress in Energy and Combustion Science*, 8(2), 135-158.
- Holm-Nielsen, J.B., Al Seadi, T., Oleskowicz-Popiel, P. 2009. The future of anaerobic digestion and biogas utilization. *Bioresource technology*, 100(22), 5478-5484.
- Hou, Z., Wang, X., Ikeda, T., Terakura, K., Oshima, M., Kakimoto, M.-a., Miyata, S. 2012. Interplay between nitrogen dopants and native point defects in graphene. *Physical Review. B*, 85(16), 165439.
- Hu, X., Lei, L., Chu, H.P., Yue, P.L. 1999. Copper/activated carbon as catalyst for organic wastewater treatment. *Carbon*, 37(4), 631-637.
- Huai, X., Xu, W., Qu, Z., Li, Z., Zhang, F., Xiang, G., Zhu, S., Chen, G. 2008. Numerical simulation of municipal solid waste combustion in a novel two-stage reciprocating incinerator. *Waste Management*, 28(1), 15-29.
- Iida, T., Amano, Y., Machida, M., Imazeki, F. 2013. Effect of surface property of activated carbon on adsorption of nitrate ion. *Chem Pharm Bull (Tokyo)*, 61(11), 1173-7.
- Isvoranu, C., Åhlund, J., Wang, B., Ataman, E., Mårtensson, N., Puglia, C., Andersen, J.N., Bocquet, M.-L., Schnadt, J. 2009. Electron spectroscopy study of the initial stages of iron

phthalocyanine growth on highly oriented pyrolytic graphite. *Journal of Chemical Physics*, 131(21), 214709.

Jafri, R.I., Rajalakshmi, N., Ramaprabhu, S. 2010. Nitrogen doped graphene nanoplatelets as catalyst support for oxygen reduction reaction in proton exchange membrane fuel cell. *Journal of Materials Chemistry*, 20(34), 7114-7117.

Jiang, A., Zhang, T., Zhao, Q.-B., Li, X., Chen, S., Frear, C.S. 2014. Evaluation of an integrated ammonia stripping, recovery, and biogas scrubbing system for use with anaerobically digested dairy manure. *Biosystems Engineering*, 119, 117-126.

Jiang, C., Jia, L., He, Y., Zhang, B., Kirumba, G., Xie, J. 2013. Adsorptive removal of phosphorus from aqueous solution using sponge iron and zeolite. *Journal of Colloid and Interface Science*, 402, 246-252.

Kabir, S., Artyushkova, K., Serov, A., Kiefer, B., Atanassov, P. 2016. Binding energy shifts for nitrogen-containing graphene-based electrocatalysts—experiments and DFT calculations. *Surface and Interface Analysis*, 48(5), 293-300.

Kadirvelu, K., Kavipriya, M., Karthika, C., Radhika, M., Vennilamani, N., Pattabhi, S. 2003. Utilization of various agricultural wastes for activated carbon preparation and application for the removal of dyes and metal ions from aqueous solutions. *Bioresource technology*, 87(1), 129-132.

Kaparaju, P., Rintala, J. 2011. Mitigation of greenhouse gas emissions by adopting anaerobic digestion technology on dairy, sow and pig farms in Finland. *Renewable Energy*, 36(1), 31-41.

Karimaian, K.A., Amrane, A., Kazemian, H., Panahi, R., Zarrabi, M. 2013. Retention of phosphorous ions on natural and engineered waste pumice: Characterization, equilibrium, competing ions, regeneration, kinetic, equilibrium and thermodynamic study. *Applied Surface Science*, 284, 419-431.

Keiluweit, M., Kleber, M., Sparrow, M.A., Simoneit, B.R., Prahl, F.G. 2012. Solvent-extractable polycyclic aromatic hydrocarbons in biochar: influence of pyrolysis temperature and feedstock. *Environmental science & technology*, 46(17), 9333-9341.

Kemp, K.C., Chandra, V., Saleh, M., Kim, K.S. 2013. Reversible CO₂ adsorption by an activated nitrogen doped graphene/polyaniline material. *Nanotechnology*, 24(23), 235703.

Kim, H., Lee, K., Woo, S.I., Jung, Y. 2011. On the mechanism of enhanced oxygen reduction reaction in nitrogen-doped graphene nanoribbons. *Physical Chemistry Chemical Physics*, 13(39), 17505-17510.

Kleerebezem, R., Mendezà, R. 2002. Autotrophic denitrification for combined hydrogen sulfide removal from biogas and post-denitrification. *Water Science and Technology*, 45(10), 349-356.

Kloss, S., Zehetner, F., Dellantonio, A., Hamid, R., Ottner, F., Liedtke, V., Schwanninger, M., Gerzabek, M.H., Soja, G. 2012. Characterization of slow pyrolysis biochars: effects of

feedstocks and pyrolysis temperature on biochar properties. *Journal of environmental quality*, 41(4), 990-1000.

Krasheninnikov, A., Banhart, F. 2007. Engineering of nanostructured carbon materials with electron or ion beams. *Nature materials*, 6(10), 723.

Kresse, G., Furthmüller, J. 1996a. Efficiency of ab-initio total energy calculations for metals and semiconductors using a plane-wave basis set. *Computation Materials Science*, 6(1), 15-50.

Kresse, G., Furthmüller, J. 1996b. Efficient iterative schemes for ab initio total-energy calculations using a plane-wave basis set. *Physical Review. B*, 54(16), 11169.

Kresse, G., Hafner, J. 1993. Ab initio molecular dynamics for liquid metals. *Physical Review. B*, 47(1), 558.

Kresse, G., Joubert, D. 1999. From ultrasoft pseudopotentials to the projector augmented-wave method. *Physical Review. B*, 59(3), 1758.

Krishnan, K.A., Haridas, A. 2008. Removal of phosphate from aqueous solutions and sewage using natural and surface modified coir pith. *Journal of Hazardous Materials*, 152(2), 527-535.

Lahaye, J., Nanse, G., Bagreev, A., Strelko, V. 1999. Porous structure and surface chemistry of nitrogen containing carbons from polymers. *Carbon*, 37(4), 585-590.

Lai, L., Potts, J.R., Zhan, D., Wang, L., Poh, C.K., Tang, C., Gong, H., Shen, Z., Lin, J., Ruoff, R.S. 2012. Exploration of the active center structure of nitrogen-doped graphene-based catalysts for oxygen reduction reaction. *Energy & Environmental Science*, 5(7), 7936-7942.

Lalley, J., Han, C., Li, X., Dionysiou, D.D., Nadagouda, M.N. 2016. Phosphate adsorption using modified iron oxide-based sorbents in lake water: Kinetics, equilibrium, and column tests. *Chemical Engineering Journal*, 284, 1386-1396.

Lambin, P., Amara, H., Ducastelle, F., Henrard, L. 2012. Long-range interactions between substitutional nitrogen dopants in graphene: electronic properties calculations. *Physical Review. B*, 86(4), 045448.

Latos, M., Karageorgos, P., Kalogerakis, N., Lazaridis, M. 2011. Dispersion of odorous gaseous compounds emitted from wastewater treatment plants. *Water, Air, & Soil Pollution*, 215(1-4), 667-677.

Lee, D.H., Lee, W.J., Lee, W.J., Kim, S.O., Kim, Y.-H. 2011. Theory, synthesis, and oxygen reduction catalysis of Fe-porphyrin-like carbon nanotube. *Physical review letters*, 106(17), 175502.

Lee, E.Y., Lee, N.Y., Cho, K.-S., Ryu, H.W. 2006. Removal of hydrogen sulfide by sulfate-resistant *Acidithiobacillus thiooxidans* AZ11. *Journal of bioscience and bioengineering*, 101(4), 309-314.

- Lee, G.-D., Wang, C., Yoon, E., Hwang, N.-M., Kim, D.-Y., Ho, K. 2005. Diffusion, coalescence, and reconstruction of vacancy defects in graphene layers. *Physical review letters*, 95(20), 205501.
- Lee, H.M., Youn, I.S., Saleh, M., Lee, J.W., Kim, K.S. 2015. Interactions of CO₂ with various functional molecules. *Physical Chemistry Chemical Physics*, 17(16), 10925-10933.
- Lee, S., Lee, M., Chung, Y.-C. 2013. Geometric and magnetic properties of Co adatom decorated nitrogen-doped graphene. *Journal of Applied Physics*, 113(17), 17B503.
- Lefèvre, M., Proietti, E., Jaouen, F., Dodelet, J.-P. 2009. Iron-based catalysts with improved oxygen reduction activity in polymer electrolyte fuel cells. *Science*, 324(5923), 71-74.
- Lehmann, J. 2007. A handful of carbon. *Nature*, 447(7141), 143-144.
- Lehmann, J., da Silva, J.P., Steiner, C., Nehls, T., Zech, W., Glaser, B. 2003. Nutrient availability and leaching in an archaeological Anthrosol and a Ferralsol of the Central Amazon basin: fertilizer, manure and charcoal amendments. *Plant and Soil*, 249(2), 343-357.
- Li, B., Boiarkina, I., Yu, W., Huang, H.M., Munir, T., Wang, G.Q., Young, B.R. 2019. Phosphorous recovery through struvite crystallization: Challenges for future design. *Science of The Total Environment*, 648, 1244-1256.
- Li, L., Quinlivan, P.A., Knappe, D.R. 2002. Effects of activated carbon surface chemistry and pore structure on the adsorption of organic contaminants from aqueous solution. *Carbon*, 40(12), 2085-2100.
- Li, M., Zhang, L., Xu, Q., Niu, J., Xia, Z. 2014. N-doped graphene as catalysts for oxygen reduction and oxygen evolution reactions: Theoretical considerations. *Journal of Catalysis*, 314, 66-72.
- Li, R., Wang, J.J., Zhou, B., Awasthi, M.K., Ali, A., Zhang, Z., Gaston, L.A., Lahori, A.H., Mahar, A. 2016a. Enhancing phosphate adsorption by Mg/Al layered double hydroxide functionalized biochar with different Mg/Al ratios. *Science of The Total Environment*, 559, 121-129.
- Li, R., Wang, J.J., Zhou, B., Awasthi, M.K., Ali, A., Zhang, Z., Lahori, A.H., Mahar, A. 2016b. Recovery of phosphate from aqueous solution by magnesium oxide decorated magnetic biochar and its potential as phosphate-based fertilizer substitute. *Bioresource Technology*, 215, 209-214.
- Li, Y., Wang, J., Li, X., Liu, J., Geng, D., Yang, J., Li, R., Sun, X. 2011. Nitrogen-doped carbon nanotubes as cathode for lithium-air batteries. *Electrochemistry Communications*, 13(7), 668-672.
- Liang, J., Jiao, Y., Jaroniec, M., Qiao, S.Z. 2012. Sulfur and nitrogen dual-doped mesoporous graphene electrocatalyst for oxygen reduction with synergistically enhanced performance. *Angewandte Chemie, International Edition in English*, 124(46), 11664-11668.

- Lin, Y.-C., Lin, C.-Y., Chiu, P.-W. 2010. Controllable graphene N-doping with ammonia plasma. *Applied Physics Letters*, 96(13), 133110.
- Liu, J.-Y., Chang, H.-Y., Truong, Q.D., Ling, Y.-C. 2013. Synthesis of nitrogen-doped graphene by pyrolysis of ionic-liquid-functionalized graphene. *Journal of Materials Chemistry* 1(9), 1713-1716.
- Liu, Y., Yu, L., Ong, C.N., Xie, J. 2016. Nitrogen-doped graphene nanosheets as reactive water purification membranes. *Nano Research*, 9(7), 1983-1993.
- Lu, B., Smart, T.J., Qin, D., Lu, J.E., Wang, N., Chen, L., Peng, Y., Ping, Y., Chen, S. 2017. Nitrogen and iron-codoped carbon hollow nanotubules as high-performance catalysts toward oxygen reduction reaction: a combined experimental and theoretical study. *Chemistry of Materials*, 29(13), 5617-5628.
- Lu, Y.-H., Zhou, M., Zhang, C., Feng, Y.-P. 2009. Metal-embedded graphene: a possible catalyst with high activity. *The Journal of Physical Chemistry. C*, 113(47), 20156-20160.
- Luo, W., Wang, B., Heron, C.G., Allen, M.J., Morre, J., Maier, C.S., Stickle, W.F., Ji, X. 2014. Pyrolysis of cellulose under ammonia leads to nitrogen-doped nanoporous carbon generated through methane formation. *Nano letters*, 14(4), 2225-2229.
- Lv, R., Li, Q., Botello-Méndez, A.R., Hayashi, T., Wang, B., Berkdemir, A., Hao, Q., Elías, A.L., Cruz-Silva, R., Gutiérrez, H.R. 2012. Nitrogen-doped graphene: beyond single substitution and enhanced molecular sensing. *Scientific reports*, 2, 586.
- Lv, R., Terrones, M. 2012. Towards new graphene materials: doped graphene sheets and nanoribbons. *Materials Letters*, 78, 209-218.
- Ma, C., Shao, X., Cao, D. 2012. Nitrogen-doped graphene nanosheets as anode materials for lithium ion batteries: a first-principles study. *Journal of Materials Chemistry*, 22(18), 8911-8915.
- MacConnell, C., Collins, H. 2007. Utilization of re-processed anaerobically digested fiber from dairy manure as a container media substrate. *International Symposium on Growing Media 2007* 819. pp. 279-286.
- Malik, P. 2004. Dye removal from wastewater using activated carbon developed from sawdust: adsorption equilibrium and kinetics. *Journal of hazardous materials*, 113(1-3), 81-88.
- Mangun, C.L., Benak, K.R., Economy, J., Foster, K.L. 2001. Surface chemistry, pore sizes and adsorption properties of activated carbon fibers and precursors treated with ammonia. *Carbon*, 39(12), 1809-1820.
- Marris, E. 2006. Putting the carbon back: Black is the new green. *Nature*, 442(7103), 624-626.

- Mehmood, F., Pachter, R., Lu, W., Boeckl, J.J. 2013. Adsorption and diffusion of oxygen on single-layer graphene with topological defects. *The Journal of Physical Chemistry* 117(20), 10366-10374.
- Meyer, J.C., Kisielowski, C., Erni, R., Rossell, M.D., Crommie, M., Zettl, A. 2008. Direct imaging of lattice atoms and topological defects in graphene membranes. *Nano letters*, 8(11), 3582-3586.
- Mohamed, B.A., Ellis, N., Kim, C.S., Bi, X., Emam, A.E.-r. 2016. Engineered biochar from microwave-assisted catalytic pyrolysis of switchgrass for increasing water-holding capacity and fertility of sandy soil. *Science of the Total Environment*, 566, 387-397.
- Momma, K., Izumi, F. 2011. VESTA 3 for three-dimensional visualization of crystal, volumetric and morphology data. *Journal of Applied Crystallography*, 44(6), 1272-1276.
- Monkhorst, H.J., Pack, J.D. 1976. Special points for Brillouin-zone integrations. *Physical Review. B*, 13(12), 5188.
- Montes-Morán, M., Suárez, D., Menéndez, J., Fuente, E. 2004. On the nature of basic sites on carbon surfaces: an overview. *Carbon*, 42(7), 1219-1225.
- Nandi, M., Okada, K., Dutta, A., Bhaumik, A., Maruyama, J., Derks, D., Uyama, H. 2012. Unprecedented CO₂ uptake over highly porous N-doped activated carbon monoliths prepared by physical activation. *Chemical Communications*, 48(83), 10283-10285.
- Nishimura, S., Yoda, M. 1997. Removal of hydrogen sulfide from an anaerobic biogas using a bio-scrubber. *Water Science and Technology*, 36(6-7), 349-356.
- Novais, S.V., Zenero, M.D.O., Barreto, M.S.C., Montes, C.R., Cerri, C.E.P. 2018. Phosphorus removal from eutrophic water using modified biochar. *Science of The Total Environment*, 633, 825-835.
- Novak, J.M., Lima, I., Xing, B., Gaskin, J.W., Steiner, C., Das, K., Ahmedna, M., Rehrh, D., Watts, D.W., Busscher, W.J. 2009. Characterization of designer biochar produced at different temperatures and their effects on a loamy sand. *Annals of Environmental Science*.
- Olsson, M., Kjällstrand, J., Petersson, G. 2003. Oxidative pyrolysis of integral softwood pellets. *Journal of analytical and applied pyrolysis*, 67(1), 135-141.
- Olsson, M., Ramnäs, O., Petersson, G. 2004. Specific volatile hydrocarbons in smoke from oxidative pyrolysis of softwood pellets. *Journal of analytical and applied pyrolysis*, 71(2), 847-854.
- Ota, K., Amano, Y., Aikawa, M., Machida, M. 2013. Removal of nitrate ions from water by activated carbons (ACs)—Influence of surface chemistry of ACs and coexisting chloride and sulfate ions. *Applied Surface Science*, 276, 838-842.

- Ozaki, J.-i. 2006. Simultaneous doping of boron and nitrogen into a carbon to enhance its oxygen reduction activity in proton exchange membrane fuel cells. *Carbon*, 44, 3358.
- Pan, S.-Y., Du, M.A., Huang, I.T., Liu, I.H., Chang, E.E., Chiang, P.-C. 2015. Strategies on implementation of waste-to-energy (WTE) supply chain for circular economy system: a review. *Journal of Cleaner Production*, 108, 409-421.
- Parambath, V.B., Nagar, R., Ramaprabhu, S. 2012. Effect of nitrogen doping on hydrogen storage capacity of palladium decorated graphene. *Langmuir*, 28(20), 7826-7833.
- Paris, O., Zollfrank, C., Zickler, G.A. 2005. Decomposition and carbonisation of wood biopolymers—a microstructural study of softwood pyrolysis. *Carbon*, 43(1), 53-66.
- Pecha, B., Arauzo, P., Garcia-Perez, M. 2015. Impact of combined acid washing and acid impregnation on the pyrolysis of Douglas fir wood. *Journal of analytical and applied pyrolysis*, 114, 127-137.
- Pelaez-Samaniego, M.R., Hummel, R.L., Liao, W., Ma, J., Jensen, J., Kruger, C., Frear, C. 2017. Approaches for adding value to anaerobically digested dairy fiber. *Renewable and Sustainable Energy Reviews*, 72, 254-268.
- Perdew, J.P., Burke, K., Ernzerhof, M. 1996. Generalized gradient approximation made simple. *Physical review letters*, 77(18), 3865.
- Proietti, E., Jaouen, F., Lefèvre, M., Larouche, N., Tian, J., Herranz, J., Dodelet, J.-P. 2011. Iron-based cathode catalyst with enhanced power density in polymer electrolyte membrane fuel cells. *Nature communications*, 2, 416.
- Pulido, A., Boronat, M., Corma, A. 2011. Theoretical investigation of gold clusters supported on graphene sheets. *New Journal of Chemistry*, 35(10), 2153-2161.
- Qu, L., Liu, Y., Baek, J.-B., Dai, L. 2010. Nitrogen-doped graphene as efficient metal-free electrocatalyst for oxygen reduction in fuel cells. *ACS nano*, 4(3), 1321-1326.
- Rad, A.S., Shadravan, A., Soleymani, A.A., Motaghedi, N. 2015. Lewis acid-base surface interaction of some boron compounds with N-doped graphene; first principles study. *Current Applied Physics*, 15(10), 1271-1277.
- Reddy, A.L.M., Srivastava, A., Gowda, S.R., Gullapalli, H., Dubey, M., Ajayan, P.M. 2010. Synthesis of nitrogen-doped graphene films for lithium battery application. *ACS nano*, 4(11), 6337-6342.
- Reich, R., Ziegler, W.T., Rogers, K.A. 1980. Adsorption of methane, ethane, and ethylene gases and their binary and ternary mixtures and carbon dioxide on activated carbon at 212-301 K and pressures to 35 atmospheres. *Industrial and Engineering Chemistry* 19(3), 336-344.

- Rico, J., García, H., Rico, C., Tejero, I. 2007. Characterisation of solid and liquid fractions of dairy manure with regard to their component distribution and methane production. *Bioresource technology*, 98(5), 971-979.
- Rittmann, B.E., Mayer, B., Westerhoff, P., Edwards, M. 2011. Capturing the lost phosphorus. *Chemosphere*, 84(6), 846-853.
- Rodriguez-Manzo, J.A., Banhart, F. 2009. Creation of individual vacancies in carbon nanotubes by using an electron beam of 1 Å diameter. *Nano letters*, 9(6), 2285-2289.
- Ronsse, F., Van Hecke, S., Dickinson, D., Prins, W. 2013. Production and characterization of slow pyrolysis biochar: influence of feedstock type and pyrolysis conditions. *Gcb Bioenergy*, 5(2), 104-115.
- Sadhvani, N., Adhikari, S., Eden, M.R. 2016. Biomass Gasification Using Carbon Dioxide: Effect of Temperature, CO₂/C Ratio, and the Study of Reactions Influencing the Process. *Industrial & engineering chemistry research*, 55(10), 2883-2891.
- Sahu, V., Grover, S., Tulachan, B., Sharma, M., Srivastava, G., Roy, M., Saxena, M., Sethy, N., Bhargava, K., Philip, D. 2015. Heavily nitrogen doped, graphene supercapacitor from silk cocoon. *Electrochimica Acta*, 160, 244-253.
- Saleh, M., Chandra, V., Kemp, K.C., Kim, K.S. 2013. Synthesis of N-doped microporous carbon via chemical activation of polyindole-modified graphene oxide sheets for selective carbon dioxide adsorption. *Nanotechnology*, 24(25), 255702.
- Schimmelpfennig, S., Glaser, B. 2012. One step forward toward characterization: some important material properties to distinguish biochars. *Journal of environmental quality*, 41(4), 1001-1013.
- Shang, G., Li, Q., Liu, L., Chen, P., Huang, X. 2016. Adsorption of hydrogen sulfide by biochars derived from pyrolysis of different agricultural/forestry wastes. *Journal of the Air & Waste Management Association*, 66(1), 8-16.
- Shang, G., Shen, G., Liu, L., Chen, Q., Xu, Z. 2013. Kinetics and mechanisms of hydrogen sulfide adsorption by biochars. *Bioresource technology*, 133, 495-499.
- Shao, Y., Sui, J., Yin, G., Gao, Y. 2008. Nitrogen-doped carbon nanostructures and their composites as catalytic materials for proton exchange membrane fuel cell. *Applied Catalysis. B, Environmental*, 79(1), 89-99.
- Shao, Y., Wang, X., Engelhard, M., Wang, C., Dai, S., Liu, J., Yang, Z., Lin, Y. 2010. Nitrogen-doped mesoporous carbon for energy storage in vanadium redox flow batteries. *Journal of Power Sources*, 195(13), 4375-4379.

- Sheets, J.P., Yang, L., Ge, X., Wang, Z., Li, Y. 2015. Beyond land application: emerging technologies for the treatment and reuse of anaerobically digested agricultural and food waste. *Waste Management*, 44, 94-115.
- Sheng, Z.-H., Shao, L., Chen, J.-J., Bao, W.-J., Wang, F.-B., Xia, X.-H. 2011. Catalyst-free synthesis of nitrogen-doped graphene via thermal annealing graphite oxide with melamine and its excellent electrocatalysis. *ACS nano*, 5(6), 4350-4358.
- Sika, M.P. 2012. Effect of biochar on chemistry, nutrient uptake and fertilizer mobility in sandy soil, Stellenbosch: Stellenbosch University.
- Singh, B.P., Hatton, B.J., Singh, B., Cowie, A.L., Kathuria, A. 2010. Influence of biochars on nitrous oxide emission and nitrogen leaching from two contrasting soils. *Journal of environmental quality*, 39(4), 1224-1235.
- Siriwardane, R.V., Shen, M.-S., Fisher, E.P., Poston, J.A. 2001. Adsorption of CO₂ on molecular sieves and activated carbon. *Energy & Fuels*, 15(2), 279-284.
- Smith, M., Scudiero, L., Espinal, J., McEwen, J.-S., Garcia-Perez, M. 2016a. Improving the deconvolution and interpretation of XPS spectra from chars by ab initio calculations. *Carbon*, 110, 155-171.
- Smith, M.W., Dallmeyer, I., Johnson, T.J., Brauer, C.S., McEwen, J.-S., Espinal, J.F., Garcia-Perez, M. 2016b. Structural analysis of char by Raman spectroscopy: Improving band assignments through computational calculations from first principles. *Carbon*, 100, 678-692.
- Smith, M.W., Pecha, B., Helms, G., Scudiero, L., Garcia-Perez, M. 2017. Chemical and morphological evaluation of chars produced from primary biomass constituents: Cellulose, xylan, and lignin. *Biomass and Bioenergy*, 104, 17-35.
- Soreanu, G., Béland, M., Falletta, P., Edmonson, K., Seto, P. 2008. Laboratory pilot scale study for H₂S removal from biogas in an anoxic biotrickling filter. *Water Science and Technology*, 57(2), 201-207.
- Speece, R.E. 1996. Anaerobic biotechnology for industrial wastewaters. in: *Anaerobic biotechnology for industrial wastewaters*.
- Streubel, J.D. 2011. Biochar: Its characterization and utility for recovering phosphorus from anaerobic digested dairy effluent. Washington State University.
- Streubel, J.D., Collins, H.P., Tarara, J.M., Cochran, R.L. 2012a. Biochar produced from anaerobically digested fiber reduces phosphorus in dairy lagoons. *Journal of environmental quality*, 41(4), 1166-1174.
- Streubel, J.D., Collins, H.P., Tarara, J.M., Cochran, R.L. 2012b. Biochar produced from anaerobically digested fiber reduces phosphorus in dairy lagoons. *J Environ Qual*, 41(4), 1166-74.

- Suliman, W., Harsh, J.B., Abu-Lail, N.I., Fortuna, A.-M., Dallmeyer, I., Garcia-Perez, M. 2016. Influence of feedstock source and pyrolysis temperature on biochar bulk and surface properties. *Biomass and Bioenergy*, 84, 37-48.
- Tamon, H., Okazaki, M. 1996. Influence of acidic surface oxides of activated carbon on gas adsorption characteristics. *Carbon*, 34(6), 741-746.
- Teater, C., Yue, Z., MacLellan, J., Liu, Y., Liao, W. 2011. Assessing solid digestate from anaerobic digestion as feedstock for ethanol production. *Bioresource technology*, 102(2), 1856-1862.
- Terrones, M., Terrones, H., Banhart, F., Charlier, J.-C., Ajayan, P. 2000. Coalescence of single-walled carbon nanotubes. *Science*, 288(5469), 1226-1229.
- Tian, G.L., Zhao, M.Q., Yu, D., Kong, X.Y., Huang, J.Q., Zhang, Q., Wei, F. 2014. Nitrogen-doped graphene/carbon nanotube hybrids: in situ formation on bifunctional catalysts and their superior electrocatalytic activity for oxygen evolution/reduction reaction. *Small*, 10(11), 2251-2259.
- Tsang, J.C., Freitag, M., Perebeinos, V., Liu, J., Avouris, P. 2007. Doping and phonon renormalization in carbon nanotubes. *Nature nanotechnology*, 2(11), 725-30.
- Ugarte, D. 1992. Curling and closure of graphitic networks under electron-beam irradiation. *Nature*, 359(6397), 707.
- Uludag-Demirer, S., Demirer, G.N., Frear, C., Chen, S. 2008. Anaerobic digestion of dairy manure with enhanced ammonia removal. *Journal of environmental management*, 86(1), 193-200.
- Uzoma, K., Inoue, M., Andry, H., Fujimaki, H., Zahoor, A., Nishihara, E. 2011. Effect of cow manure biochar on maize productivity under sandy soil condition. *Soil use and management*, 27(2), 205-212.
- Vikrant, K., Kim, K.-H., Ok, Y.S., Tsang, D.C.W., Tsang, Y.F., Giri, B.S., Singh, R.S. 2018. Engineered/designer biochar for the removal of phosphate in water and wastewater. *Science of The Total Environment*, 616-617, 1242-1260.
- Wang, H., Zhang, C., Liu, Z., Wang, L., Han, P., Xu, H., Zhang, K., Dong, S., Yao, J., Cui, G. 2011. Nitrogen-doped graphene nanosheets with excellent lithium storage properties. *Journal of Materials Chemistry*, 21(14), 5430-5434.
- Wang, J., Chen, B. 2015. Adsorption and coadsorption of organic pollutants and a heavy metal by graphene oxide and reduced graphene materials. *Chemical Engineering Journal*, 281, 379-388.
- Wang, X., Li, X., Zhang, L., Yoon, Y., Weber, P.K., Wang, H., Guo, J., Dai, H. 2009. N-doping of graphene through electrothermal reactions with ammonia. *Science*, 324(5928), 768-771.

- Wang, X., Qin, Y., Zhu, L., Tang, H. 2015a. Nitrogen-doped reduced graphene oxide as a bifunctional material for removing bisphenols: synergistic effect between adsorption and catalysis. *Environmental science & technology*, 49(11), 6855-6864.
- Wang, X., Zhu, N., Yin, B. 2008. Preparation of sludge-based activated carbon and its application in dye wastewater treatment. *Journal of hazardous materials*, 153(1-2), 22-27.
- Wang, Y., Shao, Y., Matson, D.W., Li, J., Lin, Y. 2010. Nitrogen-doped graphene and its application in electrochemical biosensing. *ACS nano*, 4(4), 1790-1798.
- Wang, Z., Guo, H., Shen, F., Yang, G., Zhang, Y., Zeng, Y., Wang, L., Xiao, H., Deng, S. 2015b. Biochar produced from oak sawdust by Lanthanum (La)-involved pyrolysis for adsorption of ammonium (NH₄⁺), nitrate (NO₃⁻), and phosphate (PO₄³⁻). *Chemosphere*, 119, 646-653.
- Wang, Z., McDonald, A.G., Westerhof, R.J., Kersten, S.R., Cuba-Torres, C.M., Ha, S., Pecha, B., Garcia-Perez, M. 2013. Effect of cellulose crystallinity on the formation of a liquid intermediate and on product distribution during pyrolysis. *Journal of analytical and applied pyrolysis*, 100, 56-66.
- Wang, Z., Qie, L., Yuan, L., Zhang, W., Hu, X., Huang, Y. 2013. Functionalized N-doped interconnected carbon nanofibers as an anode material for sodium-ion storage with excellent performance. *Carbon*, 55, 328-334.
- Warner, J.H., Rummeli, M.H., Gemming, T., Büchner, B., Briggs, G.A.D. 2008. Direct imaging of rotational stacking faults in few layer graphene. *Nano letters*, 9(1), 102-106.
- Wilkie, A.C. 2005. Anaerobic digestion: biology and benefits. *Dairy Manure Management: Treatment, Handling, and Community Relations*, 63-72.
- Wu, G., More, K.L., Johnston, C.M., Zelenay, P. 2011. High-performance electrocatalysts for oxygen reduction derived from polyaniline, iron, and cobalt. *Science*, 332(6028), 443-447.
- Wu, J., Zhang, D., Wang, Y., Hou, B. 2013. Electrocatalytic activity of nitrogen-doped graphene synthesized via a one-pot hydrothermal process towards oxygen reduction reaction. *Journal of Power Sources*, 227, 185-190.
- Xu, H., Cheng, D., Cao, D., Zeng, X.C. 2018. A universal principle for a rational design of single-atom electrocatalysts. *Nat Catal*, 10.
- Yan, H., Xu, B., Shi, S., Ouyang, C. 2012. First-principles study of the oxygen adsorption and dissociation on graphene and nitrogen doped graphene for Li-air batteries. *Journal of Applied Physics*, 112(10), 104316.
- Yang, F., Chi, C., Wang, C., Wang, Y., Li, Y. 2016. High graphite N content in nitrogen-doped graphene as an efficient metal-free catalyst for reduction of nitroarenes in water. *Green Chemistry*, 18(15), 4254-4262.

- Yang, K., Peng, J., Xia, H., Zhang, L., Srinivasakannan, C., Guo, S. 2010. Textural characteristics of activated carbon by single step CO₂ activation from coconut shells. *Journal of the Taiwan Institute of Chemical Engineers*, 41(3), 367-372.
- Yang, M., Guo, L., Hu, G., Hu, X., Xu, L., Chen, J., Dai, W., Fan, M. 2015a. Highly Cost-Effective Nitrogen-Doped Porous Coconut Shell-Based CO₂ Sorbent Synthesized by Combining Ammoxidation with KOH Activation. *Environmental Science & Technology*, 49(11), 7063-7070.
- Yang, M., Wang, L., Li, M., Hou, T., Li, Y. 2015b. Structural stability and O₂ dissociation on nitrogen-doped graphene with transition metal atoms embedded: A first-principles study. *AIP Advances*, 5(6), 067136.
- Yao, Y., Gao, B., Chen, J., Yang, L. 2013a. Engineered biochar reclaiming phosphate from aqueous solutions: mechanisms and potential application as a slow-release fertilizer. *Environmental science & technology*, 47(15), 8700-8708.
- Yao, Y., Gao, B., Chen, J., Zhang, M., Inyang, M., Li, Y., Alva, A., Yang, L. 2013b. Engineered carbon (biochar) prepared by direct pyrolysis of Mg-accumulated tomato tissues: characterization and phosphate removal potential. *Bioresource technology*, 138, 8-13.
- Yao, Y., Gao, B., Inyang, M., Zimmerman, A.R., Cao, X., Pullammanappallil, P., Yang, L. 2011a. Biochar derived from anaerobically digested sugar beet tailings: characterization and phosphate removal potential. *Bioresource technology*, 102(10), 6273-6278.
- Yao, Y., Gao, B., Inyang, M., Zimmerman, A.R., Cao, X., Pullammanappallil, P., Yang, L. 2011b. Removal of phosphate from aqueous solution by biochar derived from anaerobically digested sugar beet tailings. *Journal of hazardous materials*, 190(1), 501-507.
- Yao, Y., Gao, B., Zhang, M., Inyang, M., Zimmerman, A.R. 2012. Effect of biochar amendment on sorption and leaching of nitrate, ammonium, and phosphate in a sandy soil. *Chemosphere*, 89(11), 1467-1471.
- Ye, J., Cong, X., Zhang, P., Hoffmann, E., Zeng, G., Liu, Y., Fang, W., Wu, Y., Zhang, H. 2015. Interaction between phosphate and acid-activated neutralized red mud during adsorption process. *Applied Surface Science*, 356, 128-134.
- Yin, L.-C., Liang, J., Zhou, G.-M., Li, F., Saito, R., Cheng, H.-M. 2016. Understanding the interactions between lithium polysulfides and N-doped graphene using density functional theory calculations. *Nano Energy*, 25, 203-210.
- Yin, Q., Wang, R., Zhao, Z. 2018. Application of Mg–Al-modified biochar for simultaneous removal of ammonium, nitrate, and phosphate from eutrophic water. *Journal of Cleaner Production*, 176, 230-240.

- Yin, Q., Zhang, B., Wang, R., Zhao, Z. 2017. Biochar as an adsorbent for inorganic nitrogen and phosphorus removal from water: a review. *Environmental Science and Pollution Research*, 24(34), 26297-26309.
- Yu, D., Nagelli, E., Du, F., Dai, L. 2010. Metal-free carbon nanomaterials become more active than metal catalysts and last longer. *The journal of physical chemistry letters*, 1(14), 2165-2173.
- Yu, L., Pan, X., Cao, X., Hu, P., Bao, X. 2011. Oxygen reduction reaction mechanism on nitrogen-doped graphene: A density functional theory study. *Journal of Catalysis*, 282(1), 183-190.
- Yu, O.-Y., Raichle, B., Sink, S. 2013. Impact of biochar on the water holding capacity of loamy sand soil. *International Journal of Energy and Environmental Engineering*, 4(1), 44.
- Yu, W., Lian, F., Cui, G., Liu, Z. 2018. N-doping effectively enhances the adsorption capacity of biochar for heavy metal ions from aqueous solution. *Chemosphere*, 193, 8-16.
- Zaks, D.P.M., Winchester, N., Kucharik, C.J., Barford, C.C., Paltsev, S., Reilly, J.M. 2011. Contribution of anaerobic digesters to emissions mitigation and electricity generation under U.S. climate policy. *Environmental science & technology*, 45(16), 6735-6742.
- Zhang, C., Fu, L., Liu, N., Liu, M., Wang, Y., Liu, Z. 2011. Synthesis of nitrogen-doped graphene using embedded carbon and nitrogen sources. *Advanced Materials*, 23(8), 1020-1024.
- Zhang, C., Lai, C., Zeng, G., Huang, D., Yang, C., Wang, Y., Zhou, Y., Cheng, M. 2016. Efficacy of carbonaceous nanocomposites for sorbing ionizable antibiotic sulfamethazine from aqueous solution. *Water research*, 95, 103-112.
- Zhang, H.-p., Luo, X.-g., Lin, X.-y., Lu, X., Leng, Y., Song, H.-t. 2013a. Density functional theory calculations on the adsorption of formaldehyde and other harmful gases on pure, Ti-doped, or N-doped graphene sheets. *Applied Surface Science*, 283, 559-565.
- Zhang, L., Xia, Z. 2011. Mechanisms of oxygen reduction reaction on nitrogen-doped graphene for fuel cells. *The Journal of Physical Chemistry. C*, 115(22), 11170-11176.
- Zhang, L., Zhang, J., Wilkinson, D.P., Wang, H. 2006. Progress in preparation of non-noble electrocatalysts for PEM fuel cell reactions. *Journal of Power Sources*, 156(2), 171-182.
- Zhang, L.L., Zhao, X., Ji, H., Stoller, M.D., Lai, L., Murali, S., McDonnell, S., Cleveger, B., Wallace, R.M., Ruoff, R.S. 2012a. Nitrogen doping of graphene and its effect on quantum capacitance, and a new insight on the enhanced capacitance of N-doped carbon. *Energy & Environmental Science*, 5(11), 9618-9625.
- Zhang, M., Gao, B. 2013. Removal of arsenic, methylene blue, and phosphate by biochar/AlOOH nanocomposite. *Chemical engineering journal*, 226, 286-292.

- Zhang, M., Gao, B., Varnoosfaderani, S., Hebard, A., Yao, Y., Inyang, M. 2013. Preparation and characterization of a novel magnetic biochar for arsenic removal. *Bioresource technology*, 130, 457-462.
- Zhang, M., Gao, B., Yao, Y., Xue, Y., Inyang, M. 2012. Synthesis of porous MgO-biochar nanocomposites for removal of phosphate and nitrate from aqueous solutions. *Chemical engineering journal*, 210, 26-32.
- Zhang, T., Walawender, W.P., Fan, L.T., Fan, M., Daugaard, D., Brown, R.C. 2004. Preparation of activated carbon from forest and agricultural residues through CO₂ activation. *Chemical Engineering Journal*, 105(1), 53-59.
- Zhang, Y., Desmidt, E., Van Looveren, A., Pinoy, L., Meesschaert, B., Van der Bruggen, B. 2013c. Phosphate Separation and Recovery from Wastewater by Novel Electrodialysis. *Environmental Science & Technology*, 47(11), 5888-5895.
- Zhao, Q., Leonhardt, E., MacConnell, C., Frear, C., Chen, S. 2010. Purification technologies for biogas generated by anaerobic digestion. *Compressed Biomethane, CSANR, Ed.*
- Zheng, B., Wang, J., Wang, F.-B., Xia, X.-H. 2013a. Synthesis of nitrogen doped graphene with high electrocatalytic activity toward oxygen reduction reaction. *Electrochemistry Communications*, 28, 24-26.
- Zheng, Y., Jiao, Y., Ge, L., Jaroniec, M., Qiao, S.Z. 2013b. Two-step boron and nitrogen doping in graphene for enhanced synergistic catalysis. *Angewandte Chemie, International Edition in English*, 125(11), 3192-3198.
- Zhou, H., Meng, A., Long, Y., Li, Q., Zhang, Y. 2014. An overview of characteristics of municipal solid waste fuel in China: physical, chemical composition and heating value. *Renewable and Sustainable Energy Reviews*, 36, 107-122.
- Zhou, M., Zhai, Y., Dong, S. 2009. Electrochemical sensing and biosensing platform based on chemically reduced graphene oxide. *Analytical chemistry*, 81(14), 5603-5613.
- Zitolo, A., Goellner, V., Armel, V., Sougrati, M.-T., Mineva, T., Stievano, L., Fonda, E., Jaouen, F. 2015. Identification of catalytic sites for oxygen reduction in iron-and nitrogen-doped graphene materials. *Nature materials*, 14(9), 937.